

# An unsymmetric 4-node, 8-DOF plane membrane element perfectly breaking through MacNeal's theorem

Song Cen<sup>1,3,4,\*</sup>, Pei-Lei Zhou<sup>1</sup>, Chen-Feng Li<sup>2</sup> and Cheng-Jin Wu<sup>1</sup>

<sup>1</sup>*Department of Engineering Mechanics, School of Aerospace Engineering, Tsinghua University, Beijing 100084, China*

<sup>2</sup>*Zienkiewicz Centre for Computational Engineering & Energy Safety Research Institute, College of Engineering, Swansea University, Swansea SA2 8PP, UK*

<sup>3</sup>*High Performance Computing Center, School of Aerospace Engineering, Tsinghua University, Beijing 100084, China*

<sup>4</sup>*Key Laboratory of Applied Mechanics, School of Aerospace Engineering, Tsinghua University, Beijing 100084, China*

## SUMMARY

Among numerous finite element techniques, few models can perfectly (without any numerical problems) break through MacNeal's theorem: any 4-node, 8-DOF membrane element will either lock in in-plane bending or fail to pass a  $C_0$  patch test when the element's shape is an isosceles trapezoid. In this paper, a 4-node plane quadrilateral membrane element is developed following the unsymmetric formulation concept, which means two different sets of interpolation functions for displacement fields are simultaneously used. The first set employs the shape functions of the traditional 4-node bilinear isoparametric element, while the second set adopts a novel composite coordinate interpolation scheme with analytical trail function method, in which the Cartesian coordinates  $(x, y)$  and the second form of quadrilateral area coordinates (QACM-II)  $(S, T)$  are applied together. The resulting element US-ATFQ4 exhibits amazing performance in rigorous numerical tests. It is insensitive to various serious mesh distortions, free of trapezoidal locking, and can satisfy both the classical first-order patch test and the second-order patch test for pure bending. Furthermore, because of usage of the second form of quadrilateral area coordinates (QACM-II), the new element provides the invariance for the coordinate rotation. It seems that the behaviors of the present model are beyond the well-known contradiction defined by MacNeal's theorem. Copyright © 2015 John Wiley & Sons, Ltd.

Received 2 December 2014; Revised 27 January 2015; Accepted 29 January 2015

KEY WORDS: finite element; 4-node plane membrane element; unsymmetric formulation; analytical trial function; the second form of quadrilateral area coordinates (QACM-II); MacNeal's theorem

## 1. INTRODUCTION

Although the finite element method has been widely used in engineering and scientific computations, there are still some challenges that remain outstanding. For nearly 60 years, numerous efforts have been made to search for robust 4-node, 8-DOF (two DOFs per node) quadrilateral membrane elements that can pass the first-order (constant strain/stress ( $C_0$ )) patch test, remove parasitic shear in second-order patch test for pure bending, overcome Poisson's ratio stiffening, and are insensitive to mesh distortion. However, in 1987, MacNeal [1, 2] declared his well-known theorem, that is, any 4-node, 8-DOF plane membrane element will either lock in in-plane bending or fail to pass a  $C_0$  patch test when the element's shape is an isosceles trapezoid. This conclusion means such low-order elements must be sensitive to mesh distortion, and it almost closes out further effort to extend the linear strain capability of such elements beyond what has already been achieved for rectangular and parallelogram shapes.

\*Correspondence to: Song Cen, Department of Engineering Mechanics, School of Aerospace Engineering, Tsinghua University, Beijing 100084, China.

†E-mail: censon@tsinghua.edu.cn

MacNeal and Harder [3] proposed a famous benchmark test of thin beam bending to assess the performances of various 4-node plane quadrilateral membrane elements. As shown in Figure 1, three  $1 \times 6$  meshes with different element shapes, rectangle, parallelogram and trapezoid, are adopted; and two loading cases are considered: pure bending ( $M$ ) and transverse linear bending ( $P$ ). Although the conventional 4-node bilinear isoparametric element Q4 with full integration ( $2 \times 2$  Gauss points) can strictly pass all constant strain/stress patch tests, it will completely lock in this MacNeal's thin beam test because of the parasitic shear strains, no matter which mesh is used. In order to improve the bending behaviors of Q4, Wilson *et al.* [4] proposed the incompatible isoparametric element Q6 by introducing two internal DOFs. It can produce greatly improved results in the MacNeal's thin beam test, especially in the rectangle case, in which the precisions can reach 100% and 99.3% for loadings  $M$  and  $P$ , respectively. However, the fatal defect of the element Q6 is that it cannot pass the constant strain/stress ( $C_0$ ) patch tests and still lock in the trapezoid case. Taylor *et al.* [5] modified Q6 and constructed QM6 that can pass the  $C_0$  patch tests and keep the same accuracy in the rectangle case. But the results in the parallelogram and trapezoid cases become much worse. The commercial finite element code Abaqus [6] contains a 4-node incompatible plane quadrilateral element CPS4I (for plane stress state) or CPE4I (for plane strain state) formulated by the assumed strain method [7], whose performance is close to the element QM6. The user's manual of Abaqus [6] strongly suggests that such element be applied in bending problems only with rectangular shape. Better results for parallelogram and trapezoidal element shapes may be obtained by some other models, including the hybrid stress elements (P-S, NQ6, NQ10, SPS, and HH4- $3\beta$ ) [8–13], the generalized conforming element (GC-Q6) [14], the quasi-conforming element (QC6) [15], the improved enhanced strain elements (QE2 and QP6) [16–18], and the B-bar element [19]. But no element can break the obstacle predicted by MacNeal's theorem. Recently, by combination of finite element and mesh-free techniques, Rajendran *et al.* [20, 21] proposed a 'Finite Element (FE)–Meshfree' 4-node plane quadrilateral element that can perform well in MacNeal's thin beam test and pass the  $C_0$  patch test. But the formulations are much closer to the mesh-free methods and cannot be easily handled by usual finite element codes.

All aforementioned models are formulated in an isoparametric coordinate system. Lee and Bathe [22] have studied the influence of mesh distortions on the isoparametric membrane elements and pointed out that the nonlinear transformation between isoparametric (local) and Cartesian (global) coordinates may be the reason that leads to the sensitivity problem to mesh distortion. The assumed displacement fields may contain high order terms of  $\xi$  and  $\eta$ , but their complete order in Cartesian coordinates  $x$  and  $y$  will degrade significantly once the meshes are distorted. Therefore, although keeping compatibility between two adjacent elements formulated by the Cartesian coordinates may be difficult, the potential abilities of the Cartesian coordinates for constructing finite elements are still paid attention to. Felippa [23] designed a template formulation for 4-node plane quadrilateral element by combination of Cartesian and isoparametric coordinates. It is interesting that this element can give exact bending results for arbitrary distortions and still satisfy the  $C_0$  patch test. But, those exact bending solutions only appear in one direction and cannot be presented in other directions.

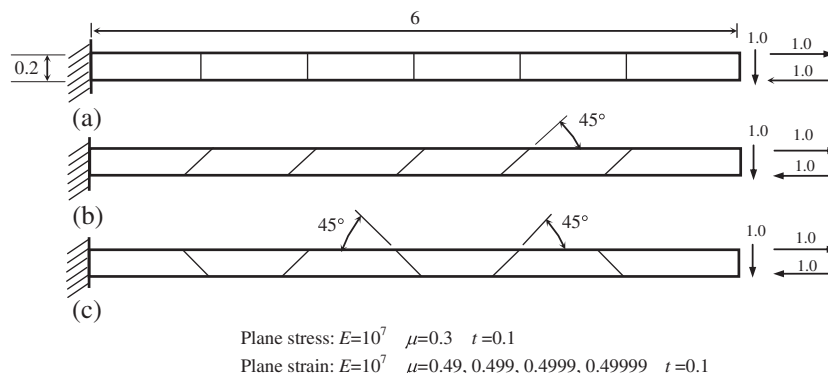


Figure 1. MacNeal's thin beam test [3]. Plane stress: (a)  $E = 10^7$ ; (b)  $\mu = 0.3$ ; and (c)  $t = 0.1$ . Plane strain: (a)  $E = 10^7$ ; (b)  $\mu = 0.49, 0.499, 0.4999, 0.49999$ ; and (c)  $t = 0.1$ .

Hence, it will not be able to meet the requirements of the bending tests, and the practical value of such element is rather limited [24]. Dasgupta [25, 26] proposed a 4-node, 8-DOF plane element with shape functions in Cartesian or physical coordinates and claimed that this element is free of trapezoidal locking, satisfies both the  $C_0$  patch test and the pure bending test. However, Fotiu [24] strictly proved that all these conclusions are wrong. Actually, if the basis polynomials in Cartesian coordinates are not complete, the element will lose the invariance for the coordinate rotation. This is the key reason why these elements failed.

In order to avoid the troubles caused by the nonlinear transformation between the isoparametric and Cartesian coordinates, Long *et al.* [27–30] extended the area coordinate method from triangle to quadrangle, systematically established three forms of quadrilateral area coordinate methods (QACM-I, QACM-II, and QACM-III). These quadrilateral area coordinate systems possess two distinguished features: (1) they are all local natural coordinate systems, which mean all advantages of the natural coordinates will exist in them; and (2) the relationships between quadrilateral area and Cartesian coordinates are always linear, so that no accuracy will be lost because of the coordinate transformation. By applying these new natural coordinates, several 4-node, 8-DOF plane membrane elements were developed [29–36], in which elements AGQ6-I and AGQ6-II [31] are the first two and the most representative models. AGQ6-I and AGQ6-II were constructed by combination of QACM-I and the techniques for element Q6 [4]. Unlike element Q6, they are free of trapezoidal locking in the second-order patch test for pure bending and can produce the same high precision results for MacNeal's thin beam test with all three meshes. Because of such excellent behaviors in bending problems, the formulations of these two elements have been extended to some linear and nonlinear shell applications [37–40]. However, as the prediction of MacNeal's theorem, the two elements cannot strictly pass the  $C_0$  patch test (only pass the weak form of the  $C_0$  patch test [31]). So, their convergence raised some queries and discussions [41–43]. Chen *et al.* [44] imposed some constraints on the elements to make them pass the  $C_0$  patch test, but the trapezoidal locking in bending comes back.

Prathap *et al.* [43, 45] pointed out that the unsymmetric element approach proposed by Rajendran *et al.* [46–51] may offer some hope to develop distortion-immune finite elements. This approach is derived from the virtual work principle and needs two different sets of shape functions, parametric set (in isoparametric coordinates), and metric set (in Cartesian coordinates), as the test and trial functions, respectively. The former are chosen to satisfy exactly the minimum inter-element as well as intra-element displacement continuity requirements, while the latter are chosen to satisfy the equilibrium relations and the completeness requirements in physical space. Although the resulting element stiffness matrix becomes unsymmetric, it has been shown that this is not a serious issue for most problems [46–51]. Because there is no Jacobian determinant in the final formula for evaluating the element stiffness matrix, the resulting elements are quite insensitive to severe mesh distortion. For example, the unsymmetric 8-node plane element US-QUAD8 [46] can provide exact solutions for constant (first-order) and linear (second-order) strain/stress problems using various distorted meshes with straight or curved element edges, even if the value of Jacobian determinant is negative. However, because of the inherent limitation of the usual metric shape functions, interpolation failure may take place when the element shape is distorted from a quadrangle to a triangle, and rotational frame dependence appears in higher-order problems because the metric shape functions are incomplete cubic polynomials in Cartesian coordinates. Although some remedies to this element have been considered for solving these difficulties [52], all of them are not convenient and effective for practical applications. Through introducing analytical trial functions and generalizing conforming conditions, Cen *et al.* [53] developed a new unsymmetric 8-node element US-ATFQ8 with fourth-order completed metric displacement fields in Cartesian coordinates. This element can overcome all the defects of US-QUAD8 and even produce exact solutions in linear bending problems (third-order patch test). But for 4-node, 8-DOF element, there is no successful model reported in any literature yet, because eight DOFs cannot determine a second-order (quadratic) completed metric displacement field.

In this paper, the effort for breaking through MacNeal's theorem is made again. A 4-node plane quadrilateral membrane element is developed following the unsymmetric formulation concept. The parametric set employs the shape functions of the traditional 4-node bilinear isoparametric

element, while the metric set adopts a novel composite coordinate interpolation scheme, in which  $(1, x, y)$  and two analytical solutions in terms of QACM-II  $(S, T)$  for pure bending are applied together. The resulting element US-ATFQ4 exhibits amazing performance in rigorous numerical tests. It is insensitive to various serious mesh distortions, free of trapezoidal locking and Poisson's ratio stiffening, and can satisfy both the classical first-order patch test and the second-order patch test for pure bending. Furthermore, because of usage of the local natural coordinate system QACM-II, the new element provides the invariance for the coordinate rotation. It seems that the behaviors of the proposed model are truly beyond the well-known contradiction defined by MacNeal's theorem.

## 2. QACM-II AND THE ANALYTICAL SOLUTIONS IN TERMS OF QACM-II FOR PURE BENDING

### 2.1. Brief reviews on second form of quadrilateral area coordinate method (QACM-II) [29]

Reference [29] proposed a novel quadrilateral area coordinate system with only two components, QACM-II, for developing quadrilateral finite element models. As shown in Figure 2,  $M_i (i = 1, 2, 3, 4)$  are the mid-side points of element edges  $\overline{23}$ ,  $\overline{34}$ ,  $\overline{41}$ , and  $\overline{12}$ , respectively. Then, the position of an arbitrary point P within the quadrilateral element  $\overline{1234}$  can be uniquely specified by the area coordinates  $S$  and  $T$  (QACM-II), which are defined as

$$S = 4 \frac{\Omega_1}{A}, \quad T = 4 \frac{\Omega_2}{A}, \tag{1}$$

where  $A$  is the area of the quadrilateral element,  $\Omega_1$  and  $\Omega_2$  are the *generalized areas* of  $\Delta PM_2M_4$  and  $\Delta PM_3M_1$ , respectively. The values of *generalized areas*  $\Omega_1$  and  $\Omega_2$  can be both positive and negative for  $\Delta PM_2M_4$  (or  $\Delta PM_3M_1$ ), if the permutation order of points P,  $M_2$ , and  $M_4$  (or P,  $M_3$ , and  $M_1$ ) is anticlockwise, a positive  $\Omega_1$  (or  $\Omega_2$ ) should be taken; otherwise,  $\Omega_1$  (or  $\Omega_2$ ) should be negative.

Two shape parameters  $\bar{g}_1$  and  $\bar{g}_2$  are defined here as

$$\begin{cases} \bar{g}_1 = \frac{A_{\Delta 123} - A_{\Delta 124}}{A} \\ \bar{g}_2 = \frac{A_{\Delta 234} - A_{\Delta 123}}{A} = \frac{A - A_{\Delta 124} - A_{\Delta 123}}{A} \end{cases}, \tag{2}$$

in which  $A_{\Delta 123}$ ,  $A_{\Delta 124}$ , and  $A_{\Delta 234}$  are the areas of  $\Delta 123$ ,  $\Delta 124$ , and  $\Delta 234$ , respectively. Different values of these shape parameters mean different shapes of a quadrangle. Thus, the local coordinates

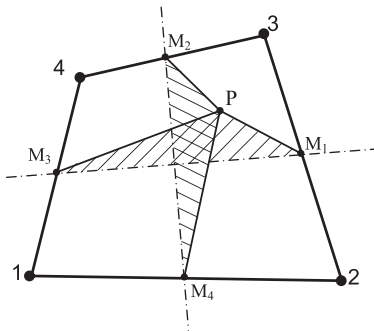


Figure 2. Definition of the quadrilateral area coordinates  $S$  and  $T$  of the second form of quadrilateral area coordinate method (QACM-II) [29].

of the corner nodes and mid-side points can be written as follows:

$$\begin{aligned} \text{node 1 : } (S_1, T_1) &= (-1 + \bar{g}_2, -1 + \bar{g}_1); & \text{node 2 : } (S_2, T_2) &= (1 - \bar{g}_2, 1 - \bar{g}_1); \\ \text{node 3 : } (S_3, T_3) &= (1 + \bar{g}_2, 1 + \bar{g}_1); & \text{node 4 : } (S_4, T_4) &= (-1 - \bar{g}_2, -1 - \bar{g}_1); \\ M_1 &: (1, 0); & M_2 &: (0, 1); \\ M_3 &: (-1, 0); & M_4 &: (0, -1). \end{aligned} \quad (3)$$

It can be observed that these coordinate values are only small modifications for isoparametric coordinates.

The relationship between QACM-II and the Cartesian coordinates is

$$\begin{cases} S = \frac{1}{A} [(a_3 - a_1) + (b_3 - b_1)x + (c_3 - c_1)y] + \bar{g}_1 = \frac{1}{A} [\bar{a}_1 + \bar{b}_1x + \bar{c}_1y] + \bar{g}_1 \\ T = \frac{1}{A} [(a_4 - a_2) + (b_4 - b_2)x + (c_4 - c_2)y] + \bar{g}_2 = \frac{1}{A} [\bar{a}_2 + \bar{b}_2x + \bar{c}_2y] + \bar{g}_2 \end{cases}, \quad (4)$$

where

$$\begin{cases} \bar{a}_1 = a_3 - a_1, & \bar{b}_1 = b_3 - b_1, & \bar{c}_1 = c_3 - c_1, \\ \bar{a}_2 = a_4 - a_2, & \bar{b}_2 = b_4 - b_2, & \bar{c}_2 = c_4 - c_2, \end{cases} \quad (5)$$

$$\begin{aligned} a_i &= x_j y_k - x_k y_j, & b_i &= y_j - y_k, & c_i &= x_k - x_j, \\ (i &= 1, 2, 3, 4; & j &= 2, 3, 4, 1; & k &= 3, 4, 1, 2) \end{aligned} \quad (6)$$

in which  $(x_i, y_i)$  ( $i = 1, 2, 3, 4$ ) are the Cartesian coordinates of the four corner nodes. The linear relationship between QACM-II and Cartesian coordinates is clearly illustrated.

And the relationship between QACM-II and isoparametric coordinates is

$$\begin{cases} S = \xi + \bar{g}_2 \xi \eta \\ T = \eta + \bar{g}_1 \xi \eta \end{cases}. \quad (7)$$

It can be seen that the new area coordinates  $S$  and  $T$  will degenerate to be the isoparametric coordinates  $\xi$  and  $\eta$  for rectangular element cases.

The transformation of first-order derivatives is

$$\begin{Bmatrix} \frac{\partial}{\partial x} \\ \frac{\partial}{\partial y} \end{Bmatrix} = \frac{1}{A} \begin{bmatrix} \bar{b}_1 & \bar{b}_2 \\ \bar{c}_1 & \bar{c}_2 \end{bmatrix} \begin{Bmatrix} \frac{\partial}{\partial S} \\ \frac{\partial}{\partial T} \end{Bmatrix}. \quad (8)$$

And the transformation of second-order derivatives is

$$\begin{Bmatrix} \frac{\partial^2}{\partial x^2} \\ \frac{\partial^2}{\partial y^2} \\ \frac{\partial^2}{\partial x \partial y} \end{Bmatrix} = \frac{1}{A^2} \begin{bmatrix} \bar{b}_1^2 & \bar{b}_2^2 & 2\bar{b}_1\bar{b}_2 \\ \bar{c}_1^2 & \bar{c}_2^2 & 2\bar{c}_1\bar{c}_2 \\ \bar{b}_1\bar{c}_1 & \bar{b}_2\bar{c}_2 & \bar{b}_1\bar{c}_2 + \bar{b}_2\bar{c}_1 \end{bmatrix} \begin{Bmatrix} \frac{\partial^2}{\partial S^2} \\ \frac{\partial^2}{\partial T^2} \\ \frac{\partial^2}{\partial S \partial T} \end{Bmatrix}. \quad (9)$$

Other proofs and formulae can be found in [29].

## 2.2. The basic analytical solutions in terms of second form of quadrilateral area coordinate method (QACM-II) for pure bending

Just as the Trefftz finite element method [54] and the hybrid stress-function element method proposed recently [55–60], the fundamental analytical solutions of governing equations in elasticity can be used as the trial functions to improve the performance of a finite element model.

In plane problem, the stress components can be expressed by the Airy stress function  $\phi$  as follows:

$$\sigma_x = \frac{\partial^2 \phi}{\partial y^2}, \quad \sigma_y = \frac{\partial^2 \phi}{\partial x^2}, \quad \tau_{xy} = -\frac{\partial^2 \phi}{\partial x \partial y}. \quad (10)$$

Then, the strains can be obtained by the stress–strain relation (generalized Hooke law)

$$\boldsymbol{\varepsilon} = \begin{Bmatrix} \varepsilon_x \\ \varepsilon_y \\ \gamma_{xy} \end{Bmatrix} = \frac{1}{E'} \begin{bmatrix} 1 & -\mu' & 0 \\ -\mu' & 1 & 0 \\ 0 & 0 & 2(1 + \mu') \end{bmatrix} \begin{Bmatrix} \sigma_x \\ \sigma_y \\ \tau_{xy} \end{Bmatrix} = \mathbf{C}\boldsymbol{\sigma}, \quad \text{for isotropic case;} \quad (11a)$$

$$\boldsymbol{\varepsilon} = \begin{Bmatrix} \varepsilon_x \\ \varepsilon_y \\ \gamma_{xy} \end{Bmatrix} = \begin{bmatrix} \hat{C}_{11} & \hat{C}_{12} & \hat{C}_{16} \\ \hat{C}_{21} & \hat{C}_{22} & \hat{C}_{26} \\ \hat{C}_{61} & \hat{C}_{62} & \hat{C}_{66} \end{bmatrix} \begin{Bmatrix} \sigma_x \\ \sigma_y \\ \tau_{xy} \end{Bmatrix} = \mathbf{C}\boldsymbol{\sigma}, \quad \text{for anisotropic case,} \quad (11b)$$

where  $\mathbf{C}$  is the elasticity matrix of compliances;  $E' = E$  and  $\mu' = \mu$  for plane stress problem, whereas  $E' = E/(1 - \mu^2)$  and  $\mu' = \mu/(1 - \mu)$  for plane strain problem, in which  $E$  and  $\mu$  are Young's modulus and Poisson's ratio, respectively;  $\hat{C}_{ij}$  ( $i, j = 1, 2, 6$ ) are the reduced elastic compliances, and their definitions can be found in [56].

By integrating the following geometrical equations:

$$\frac{\partial u}{\partial x} = \varepsilon_x, \quad \frac{\partial v}{\partial y} = \varepsilon_y, \quad \frac{\partial u}{\partial y} + \frac{\partial v}{\partial x} = \gamma_{xy}, \quad (12)$$

the displacements  $u$  and  $v$  can be obtained.

Substituting Equations (10) and (11) into the following compatibility equation of plane problem

$$\frac{\partial^2 \varepsilon_x}{\partial y^2} + \frac{\partial^2 \varepsilon_y}{\partial x^2} = \frac{\partial^2 \gamma_{xy}}{\partial x \partial y}, \quad (13)$$

yields

$$\nabla^4 \phi = \frac{\partial^4 \phi}{\partial x^4} + 2 \frac{\partial^4 \phi}{\partial x^2 \partial y^2} + \frac{\partial^4 \phi}{\partial y^4} = 0 \quad (14a)$$

for isotropic case, or

$$\hat{C}_{11} \frac{\partial^4 \phi}{\partial y^4} + \hat{C}_{22} \frac{\partial^4 \phi}{\partial x^4} + (2\hat{C}_{12} + \hat{C}_{66}) \frac{\partial^4 \phi}{\partial x^2 \partial y^2} - 2\hat{C}_{16} \frac{\partial^4 \phi}{\partial x \partial y^3} - 2\hat{C}_{26} \frac{\partial^4 \phi}{\partial x^3 \partial y} = 0 \quad (14b)$$

for anisotropic case. For any analytical solution of  $\phi$  that satisfies Equation (14), the resulting stresses, strains, and displacements will automatically satisfy all homogeneous governing equations (the boundary conditions are not considered). Reference [53] gave the first 18 linearly independent analytical solutions (from constant to fifth-order terms) of  $\phi$  and related stresses and displacements in terms of Cartesian coordinates for isotropic case, in which the displacement terms reach fourth-order completeness. Reference [56] gives 23 linearly independent analytical solutions (from quadratic to seventh-order terms) of  $\phi$  and related stresses in terms of Cartesian coordinates for anisotropic case, in which the stress terms reach fifth-order completeness. Because the relationship between QACM-II and Cartesian coordinate system is linear, the solutions in terms of the QACM-II can be easily obtained. Reference [35] presented the first 10 linearly independent analytical solutions (from constant to cubic terms) of  $\phi$  and related strains and displacements in terms of QACM-II for isotropic case, in which the displacement terms reach second-order completeness. These solutions or terms can be used as the basis functions of the interpolation formulae for assumed stresses, strains, and displacements in finite element formulations, so that they are called *the basic analytical solutions* here.

It is well known that  $\phi = a'y^3$  ( $a'$  is an undetermined coefficient) is the stress function for solving the pure bending problem of a rectangular beam shown in Figure 3(a). So, the basis function (basic analytical solution) for the stress function  $\phi$  is  $y^3$ . Similarly, for the beam shown in

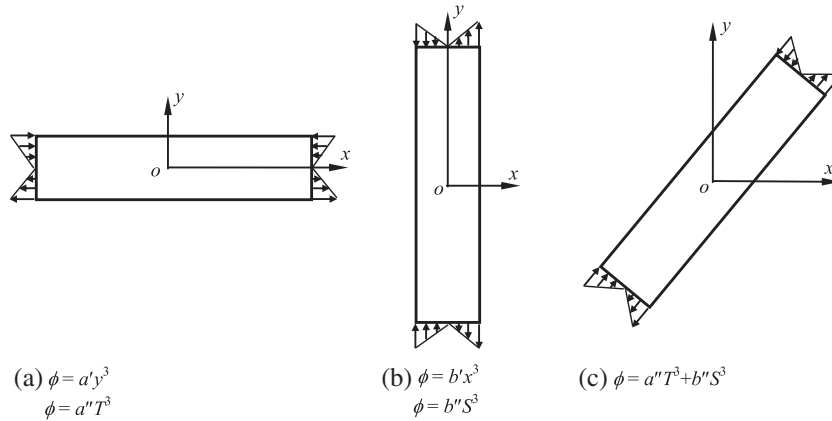


Figure 3. Pure bending problems and their stress functions. (a)  $\phi = a'y^3$ ,  $\phi = a''T^3$ ; (b)  $\phi = b'x^3$ ,  $\phi = b''S^3$ ; and (c)  $\phi = a''T^3 + b''S^3$ .

Figure 3(b), the basic analytical solution for the stress function  $\phi$  is  $x^3$ . But these solutions and resulting stresses are only correct in one direction. Once the coordinate axes rotate, the exactness will be lost (Figure 3(c)). This is because the basis functions for pure bending are not complete ( $1, x, y, x^2y$  and  $xy^2$  are missing), even the linear combination of  $(a'y^3 + b'x^3)$  cannot keep the exactness so long as the beam is not along  $x$ -direction and  $y$ -direction. That is to say, if the exact solutions for pure bending can be kept in all directions, four cubic basic analytical solutions ( $x^3, y^3, x^2y$ , and  $xy^2$ ) of the stress function must be all adopted. This brings great difficulty for developing 4-node, 8-DOF element, in which six DOFs (three DOFs for each direction) must be used for determining rigid and linear displacements, and only two DOFs are left.

The aforementioned difficulty may be broken by usage of the QACM-II ( $S$  and  $T$ ) as follows:

- (i) Both  $S^3$  and  $T^3$  satisfy Equation (14). So, they are the basic analytical solutions of the stress function  $\phi$ .
- (ii) From Equation (4), it can be easily proved that  $T$  will degenerate into  $y$  for the configuration of Figure 3(a). Therefore,  $T^3$  is also the basic analytical solution of the stress function for pure bending defined in Figure 3(a). Similarly, because  $S$  will degenerate into  $x$  for the configuration of Figure 3(b),  $S^3$  is also the basic analytical solution of the stress function for pure bending defined in Figure 3(b).
- (iii) The QACM-II,  $S$  and  $T$ , are the local natural coordinates, which mean they should possess invariance in two-dimensional space, no matter how the Cartesian coordinate axes rotate.
- (iv) From Equation (4), it can be observed that  $S^3$  and  $T^3$  will contain not only the terms of  $x^3, y^3, x^2y$ , and  $xy^2$  but also the terms of constant,  $x, y, x^2, y^2$ , and  $xy$ .

*Hypothesis:* According to the aforementioned points (i), (ii), (iii), and (iv), the linear combination  $\phi = a''T^3 + b''S^3$  (in which  $a''$  and  $b''$  are two undetermined coefficients) may reflect exact solutions for pure bending in all directions. That is,  $S^3$  and  $T^3$  should represent all the basic analytical solutions of the stress function for pure bending.

This hypothesis will be fully tested by numerical examples in Section 4. Thus, two DOFs are enough to determine the assumed displacements for pure bending. Following Equations (10)–(12), the resulting basic analytical solutions of stresses, strains, and displacements corresponding to the pure bending state can be obtained.

Let

$$f_1 = \bar{b}_1^2 + \bar{c}_1^2, \quad f_2 = \bar{b}_2^2 + \bar{c}_2^2, \quad f_3 = \bar{b}_1\bar{b}_2 + \bar{c}_1\bar{c}_2. \quad (15)$$

- (1) For  $\phi_7 = S^3$  ( $S^3$  is the seventh basic analytical solution of  $\phi$  [35])

- Isotropic case

Stresses:

$$\sigma_{x7} = \frac{6\bar{c}_1^2}{A^2} S, \sigma_{y7} = \frac{6\bar{b}_1^2}{A^2} S, \tau_{xy7} = -\frac{6\bar{b}_1\bar{c}_1}{A^2} S; \quad (16)$$

Strains:

$$\varepsilon_{x7} = \frac{6}{EA^2} [(\bar{c}_1^2 - \mu\bar{b}_1^2) S], \varepsilon_{y7} = \frac{6}{EA^2} [(\bar{b}_1^2 - \mu\bar{c}_1^2) S], \gamma_{xy7} = -\frac{12(1+\mu)\bar{b}_1\bar{c}_1}{EA^2} S; \quad (17)$$

Displacements:

$$\begin{cases} U_7 = \frac{3}{16EA^3} [(4\bar{c}_1^2\bar{c}_2A - \bar{c}_1^2\bar{b}_2f_3 - \bar{b}_1\bar{b}_2^2f_1 - 16\bar{b}_1\mu A^2) S^2 + 2\bar{b}_2f_1^2ST - \bar{b}_1f_1^2T^2] \\ V_7 = \frac{3}{16EA^3} [(-4\bar{b}_1^2\bar{b}_2A - \bar{b}_1^2\bar{c}_2f_3 - \bar{c}_1\bar{c}_2^2f_1 - 16\bar{c}_1\mu A^2) S^2 + 2\bar{c}_2f_1^2ST - \bar{c}_1f_1^2T^2] \end{cases} \quad (18)$$

- Anisotropic case

Stresses:

$$\sigma_{x7} = \frac{6\bar{c}_1^2}{A^2} S, \sigma_{y7} = \frac{6\bar{b}_1^2}{A^2} S, \tau_{xy7} = -\frac{6\bar{b}_1\bar{c}_1}{A^2} S; \quad (19)$$

Strains:

$$\begin{cases} \varepsilon_{x7} = \frac{6}{A^2} [(\bar{c}_1^2\hat{C}_{11} + \bar{b}_1^2\hat{C}_{12} - \bar{b}_1\bar{c}_1\hat{C}_{16}) S] \\ \varepsilon_{y7} = \frac{6}{A^2} [(\bar{c}_1^2\hat{C}_{21} + \bar{b}_1^2\hat{C}_{22} - \bar{b}_1\bar{c}_1\hat{C}_{26}) S]; \\ \gamma_{xy7} = \frac{6}{A^2} [(\bar{c}_1^2\hat{C}_{61} + \bar{b}_1^2\hat{C}_{62} - \bar{b}_1\bar{c}_1\hat{C}_{66}) S] \end{cases} \quad (20)$$

Displacements:

$$\begin{aligned} U_7 = \frac{3}{16A^3} \{ & [\bar{c}_1^2\bar{c}_2(4A - \bar{b}_2\bar{c}_1)\hat{C}_{11} - \bar{b}_1^3\bar{b}_2^2\hat{C}_{22} + 16\bar{b}_1A^2\hat{C}_{12} - \bar{b}_1\bar{b}_2^2\bar{c}_1^2(\hat{C}_{12} + \hat{C}_{21} + \hat{C}_{66}) \\ & - 16\bar{c}_1A^2\hat{C}_{16} + \bar{b}_2^2\bar{c}_1^3(\hat{C}_{16} + \hat{C}_{61}) + \bar{b}_1^2\bar{b}_2^2\bar{c}_1(\hat{C}_{26} + \hat{C}_{62})] S^2 + [2\bar{b}_2\bar{c}_1^4\hat{C}_{11} \\ & + 2\bar{b}_1^4\bar{b}_2\hat{C}_{22} + 2\bar{b}_1^2\bar{b}_2\bar{c}_1^2(\hat{C}_{12} + \hat{C}_{21} + \hat{C}_{66}) - 2\bar{b}_1\bar{b}_2\bar{c}_1^3(\hat{C}_{16} + \hat{C}_{61}) \\ & - 2\bar{b}_1^3\bar{b}_2\bar{c}_1(\hat{C}_{26} + \hat{C}_{62})] ST + [-\bar{b}_1\bar{c}_1^4\hat{C}_{11} - \bar{b}_1^5\hat{C}_{22} - \bar{b}_1^3\bar{c}_1^2(\hat{C}_{12} + \hat{C}_{21} + \hat{C}_{66}) \\ & + \bar{b}_1^2\bar{c}_1^3(\hat{C}_{16} + \hat{C}_{61}) + \bar{b}_1^4\bar{c}_1(\hat{C}_{26} + \hat{C}_{62})] T^2 \} \end{aligned} \quad (21a)$$

$$\begin{aligned} V_7 = \frac{3}{16A^3} \{ & [-\bar{c}_1^3\bar{c}_2^2\hat{C}_{11} - \bar{b}_1^2\bar{b}_2(4A + \bar{b}_1\bar{c}_2)\hat{C}_{22} + 16\bar{c}_1A^2\hat{C}_{21} - \bar{b}_1^2\bar{c}_1\bar{c}_2^2(\hat{C}_{12} \\ & + \hat{C}_{21} + \hat{C}_{66}) - 16\bar{b}_1A^2\hat{C}_{26} + \bar{b}_1^3\bar{c}_2^2(\hat{C}_{26} + \hat{C}_{62}) + \bar{b}_1\bar{c}_1^2\bar{c}_2^2(\hat{C}_{16} + \hat{C}_{61})] S^2 \\ & + [2\bar{c}_1^4\bar{c}_2\hat{C}_{11} + 2\bar{b}_1^4\bar{c}_2\hat{C}_{22} + 2\bar{b}_1^2\bar{c}_1^2\bar{c}_2(\hat{C}_{12} + \hat{C}_{21} + \hat{C}_{66}) - 2\bar{b}_1\bar{c}_1^3\bar{c}_2(\hat{C}_{16} + \hat{C}_{61}) \\ & - 2\bar{b}_1^3\bar{c}_1\bar{c}_2(\hat{C}_{26} + \hat{C}_{62})] ST + [-\bar{c}_1^5\hat{C}_{11} - \bar{b}_1^4\bar{c}_1\hat{C}_{22} - \bar{b}_1^2\bar{c}_1^3(\hat{C}_{12} + \hat{C}_{21} + \hat{C}_{66}) \\ & + \bar{b}_1\bar{c}_1^4(\hat{C}_{16} + \hat{C}_{61}) + \bar{b}_1^3\bar{c}_1^2(\hat{C}_{26} + \hat{C}_{62})] T^2 \} \end{aligned} \quad (21b)$$

(2) For  $\phi_8 = T^3$  ( $T^3$  is the eighth basic analytical solution of  $\phi$  [35])

- Isotropic case

Stresses:

$$\sigma_{x8} = \frac{6\bar{c}_2^2}{A^2}T, \quad \sigma_{y8} = \frac{6\bar{b}_2^2}{A^2}T, \quad \tau_{xy8} = -\frac{6\bar{b}_2\bar{c}_2}{A^2}T; \quad (22)$$

Strains:

$$\varepsilon_{x8} = \frac{6}{EA^2} [(\bar{c}_2^2 - \mu\bar{b}_2^2)T], \quad \varepsilon_{y8} = \frac{6}{EA^2} [(\bar{b}_2^2 - \mu\bar{c}_2^2)T], \quad \gamma_{xy8} = -\frac{12(1+\mu)\bar{b}_2\bar{c}_2}{EA^2}T; \quad (23)$$

Displacements:

$$\begin{cases} U_8 = \frac{3}{16EA^3} [-\bar{b}_2 f_2^2 S^2 + 2\bar{b}_1 f_2^2 ST - (4\bar{c}_2^2 \bar{c}_1 A + \bar{c}_2^2 \bar{b}_1 f_3 + \bar{b}_2 \bar{b}_1^2 f_2 + 16\bar{b}_2 \mu A^2) T^2] \\ V_8 = \frac{3}{16EA^3} [-\bar{c}_2 f_2^2 S^2 + 2\bar{c}_1 f_2^2 ST - (-4\bar{b}_2^2 \bar{b}_1 A + \bar{b}_2^2 \bar{c}_1 f_3 + \bar{c}_2 \bar{c}_1^2 f_2 + 16\bar{c}_2 \mu A^2) T^2] \end{cases} \quad (24)$$

- Anisotropic case

Stresses:

$$\sigma_{x8} = \frac{6\bar{c}_2^2}{A^2}T, \quad \sigma_{y8} = \frac{6\bar{b}_2^2}{A^2}T, \quad \tau_{xy8} = -\frac{6\bar{b}_2\bar{c}_2}{A^2}T; \quad (25)$$

Strains:

$$\begin{cases} \varepsilon_{x8} = \frac{6}{A^2} [(\bar{c}_2^2 \hat{C}_{11} + \bar{b}_2^2 \hat{C}_{12} - \bar{b}_2 \bar{c}_2 \hat{C}_{16}) T] \\ \varepsilon_{y8} = \frac{6}{A^2} [(\bar{c}_2^2 \hat{C}_{21} + \bar{b}_2^2 \hat{C}_{22} - \bar{b}_2 \bar{c}_2 \hat{C}_{26}) T] \\ \gamma_{xy8} = \frac{6}{A^2} [(\bar{c}_2^2 \hat{C}_{61} + \bar{b}_2^2 \hat{C}_{62} - \bar{b}_2 \bar{c}_2 \hat{C}_{66}) T] \end{cases} ; \quad (26)$$

Displacements:

$$\begin{aligned} U_8 = \frac{3}{16A^3} \{ & [-\bar{b}_2 \bar{c}_2^4 \hat{C}_{11} - \bar{b}_2^5 \hat{C}_{22} - \bar{b}_2^3 \bar{c}_2^2 (\hat{C}_{12} + \hat{C}_{21} + \hat{C}_{66}) + \bar{b}_2^2 \bar{c}_2^3 (\hat{C}_{16} + \hat{C}_{61}) \\ & + \bar{b}_2^4 \bar{c}_2 (\hat{C}_{26} + \hat{C}_{62})] S^2 + [2\bar{b}_1 \bar{c}_2^4 \hat{C}_{11} + 2\bar{b}_1 \bar{b}_2^4 \hat{C}_{22} + 2\bar{b}_1 \bar{b}_2^2 \bar{c}_2^2 (\hat{C}_{12} + \hat{C}_{21} + \hat{C}_{66}) \\ & - 2\bar{b}_1 \bar{b}_2 \bar{c}_2^3 (\hat{C}_{16} + \hat{C}_{61}) - 2\bar{b}_1 \bar{b}_2^3 \bar{c}_2 (\hat{C}_{26} + \hat{C}_{62})] ST + [-\bar{c}_1 \bar{c}_2^2 (4A + \bar{b}_1 \bar{c}_2) \hat{C}_{11} \\ & - \bar{b}_1^2 \bar{b}_2^3 \hat{C}_{22} + 16\bar{b}_2 A^2 \hat{C}_{12} - \bar{b}_1^2 \bar{b}_2 \bar{c}_2^2 (\hat{C}_{12} + \hat{C}_{21} + \hat{C}_{66}) - 16\bar{c}_2 A^2 \hat{C}_{16} \\ & + \bar{b}_1^2 \bar{c}_2^3 (\hat{C}_{16} + \hat{C}_{61}) + \bar{b}_1^2 \bar{b}_2^2 \bar{c}_2 (\hat{C}_{26} + \hat{C}_{62})] T^2 \} \end{aligned} \quad (27a)$$

$$\begin{aligned} V_8 = \frac{3}{16A^3} \{ & [-\bar{c}_2^5 \hat{C}_{11} - \bar{b}_2^4 \bar{c}_2 \hat{C}_{22} - \bar{b}_2^2 \bar{c}_2^3 (\hat{C}_{12} + \hat{C}_{21} + \hat{C}_{66}) + \bar{b}_2 \bar{c}_2^4 (\hat{C}_{16} + \hat{C}_{61}) \\ & + \bar{b}_2^3 \bar{c}_2^2 (\hat{C}_{26} + \hat{C}_{62})] S^2 + [2\bar{c}_1 \bar{c}_2^4 \hat{C}_{11} + 2\bar{b}_2^4 \bar{c}_1 \hat{C}_{22} + 2\bar{b}_2^2 \bar{c}_1 \bar{c}_2^2 (\hat{C}_{12} + \hat{C}_{21} + \hat{C}_{66}) \\ & - 2\bar{b}_2 \bar{c}_1 \bar{c}_2^3 (\hat{C}_{16} + \hat{C}_{61}) - 2\bar{b}_2^3 \bar{c}_1 \bar{c}_2 (\hat{C}_{26} + \hat{C}_{62})] ST + [-\bar{c}_1^2 \bar{c}_2^3 \hat{C}_{11} + \bar{b}_1 \bar{b}_2^2 (4A - \bar{b}_2 \bar{c}_1) \hat{C}_{22} \\ & + 16\bar{c}_2 A^2 \hat{C}_{21} - \bar{b}_2^2 \bar{c}_1^2 \bar{c}_2 (\hat{C}_{12} + \hat{C}_{21} + \hat{C}_{66}) - 16\bar{b}_2 A^2 \hat{C}_{26} + \bar{b}_2^3 \bar{c}_1^2 (\hat{C}_{26} + \hat{C}_{62}) \\ & + \bar{b}_2 \bar{c}_1^2 \bar{c}_2^2 (\hat{C}_{16} + \hat{C}_{61})] T^2 \} \end{aligned} \quad (27b)$$

3. CONSTRUCTION OF A NEW UNSYMMETRIC 4-NODE, 8-DOF ELEMENT US-ATFQ4

Consider a 4-node plane quadrilateral element, as shown in Figure 4. Nodes 1, 2, 3, and 4 are the corner nodes;  $(x_i, y_i) (i = 1, 2, 3, 4)$  are the Cartesian coordinates of the four corner nodes;  $u_i$  and  $v_i (i = 1, 2, 3, 4)$  are the nodal displacements along  $x$ -direction and  $y$ -direction, respectively. The element nodal displacement vector  $\mathbf{q}^e$  is given in

$$\mathbf{q}^e = [u_1 \ v_1 \ u_2 \ v_2 \ u_3 \ v_3 \ u_4 \ v_4]^T. \tag{28}$$

Two sets of the assumed displacement fields are considered. The first set is the parametric displacement fields and assumed as

$$\bar{\mathbf{u}} = \begin{Bmatrix} \bar{u} \\ \bar{v} \end{Bmatrix} = \bar{\mathbf{N}}\mathbf{q}^e, \tag{29}$$

where

$$\bar{\mathbf{N}} = \begin{bmatrix} \bar{N}_1 & 0 & \bar{N}_2 & 0 & \bar{N}_3 & 0 & \bar{N}_4 & 0 \\ 0 & \bar{N}_1 & 0 & \bar{N}_2 & 0 & \bar{N}_3 & 0 & \bar{N}_4 \end{bmatrix}, \tag{30}$$

with

$$\begin{cases} \bar{N}_1 = \frac{1}{4}(1 - \xi)(1 - \eta) \\ \bar{N}_2 = \frac{1}{4}(1 + \xi)(1 - \eta) \\ \bar{N}_3 = \frac{1}{4}(1 + \xi)(1 + \eta) \\ \bar{N}_4 = \frac{1}{4}(1 - \xi)(1 + \eta) \end{cases}. \tag{31}$$

Obviously, they are just the displacement fields of the traditional 4-node bilinear isoparametric element Q4 and satisfy exactly the minimum inter-element as well as intra-element displacement continuity requirements. Then, the corresponding strain fields are

$$\bar{\boldsymbol{\epsilon}} = \begin{Bmatrix} \bar{\epsilon}_x \\ \bar{\epsilon}_y \\ \bar{\gamma}_{xy} \end{Bmatrix} = \bar{\mathbf{B}}\mathbf{q}^e, \tag{32}$$

where  $\bar{\mathbf{B}}$  is the strain matrix, and

$$\bar{\mathbf{B}} = \begin{bmatrix} \bar{N}_{1,x} & 0 & \bar{N}_{2,x} & 0 & \bar{N}_{3,x} & 0 & \bar{N}_{4,x} & 0 \\ 0 & \bar{N}_{1,y} & 0 & \bar{N}_{2,y} & 0 & \bar{N}_{3,y} & 0 & \bar{N}_{4,y} \\ \bar{N}_{1,y} & \bar{N}_{1,x} & \bar{N}_{2,y} & \bar{N}_{2,x} & \bar{N}_{3,y} & \bar{N}_{3,x} & \bar{N}_{4,y} & \bar{N}_{4,x} \end{bmatrix} = \frac{1}{|\mathbf{J}|}\bar{\mathbf{B}}^*, \tag{33}$$

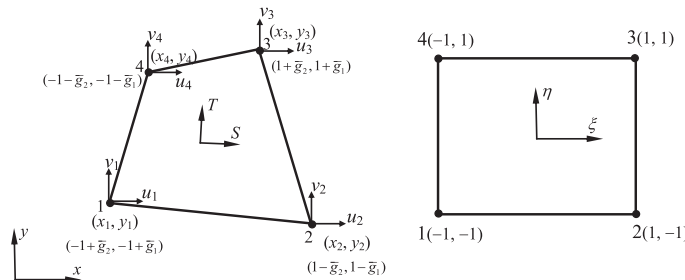


Figure 4. A 4-node plane quadrilateral element.

with

$$\bar{\mathbf{B}}^* = [\bar{\mathbf{B}}_1^* \bar{\mathbf{B}}_2^* \bar{\mathbf{B}}_3^* \bar{\mathbf{B}}_4^*], \tag{34}$$

$$\bar{\mathbf{B}}_i^* = \begin{bmatrix} \frac{\partial y}{\partial \eta} \frac{\partial \bar{N}_i}{\partial \xi} - \frac{\partial y}{\partial \xi} \frac{\partial \bar{N}_i}{\partial \eta} & 0 \\ 0 & -\frac{\partial x}{\partial \eta} \frac{\partial \bar{N}_i}{\partial \xi} + \frac{\partial x}{\partial \xi} \frac{\partial \bar{N}_i}{\partial \eta} \\ -\frac{\partial x}{\partial \eta} \frac{\partial \bar{N}_i}{\partial \xi} + \frac{\partial x}{\partial \xi} \frac{\partial \bar{N}_i}{\partial \eta} & \frac{\partial y}{\partial \eta} \frac{\partial \bar{N}_i}{\partial \xi} - \frac{\partial y}{\partial \xi} \frac{\partial \bar{N}_i}{\partial \eta} \end{bmatrix}, (i = 1, 2, 3, 4), \tag{35}$$

$$x = \sum_{i=1}^4 \bar{N}_i x_i, \quad y = \sum_{i=1}^4 \bar{N}_i y_i, \tag{36}$$

and  $|\mathbf{J}|$  is the Jacobian determinant,

$$|\mathbf{J}| = \frac{\partial x}{\partial \xi} \frac{\partial y}{\partial \eta} - \frac{\partial x}{\partial \eta} \frac{\partial y}{\partial \xi}. \tag{37}$$

The second set of displacement fields is assumed as follows:

$$\hat{\mathbf{u}} = \begin{Bmatrix} \hat{u} \\ \hat{v} \end{Bmatrix} = \mathbf{P}\boldsymbol{\alpha} = \begin{bmatrix} 1 & 0 & x & 0 & y & 0 & U_7 & U_8 \\ 0 & 1 & 0 & x & 0 & y & V_7 & V_8 \end{bmatrix} \begin{Bmatrix} \alpha_1 \\ \alpha_2 \\ \alpha_3 \\ \vdots \\ \alpha_8 \end{Bmatrix}, \tag{38}$$

where  $\alpha_i$  ( $i = 1-8$ ) are eight undetermined coefficients;  $U_7, V_7, U_8,$  and  $V_8$  are the displacement solutions derived from  $\phi_7 = S^3$  and  $\phi_8 = T^3$ , respectively.  $U_7$  and  $V_7$  are given in Equation (18) or (21), and  $U_8$  and  $V_8$  are given in Equation (24) or (27). This is a typical analytical trial function method.

Substitution of Cartesian and quadrilateral area coordinates of four nodes into Equation (38) yields

$$\hat{\mathbf{d}} \boldsymbol{\alpha} = \mathbf{q}^e, \tag{39}$$

in which

$$\hat{\mathbf{d}} = \begin{bmatrix} \mathbf{P}(x_1, y_1, S_1, T_1) \\ \mathbf{P}(x_2, y_2, S_2, T_2) \\ \mathbf{P}(x_3, y_3, S_3, T_3) \\ \mathbf{P}(x_4, y_4, S_4, T_4) \end{bmatrix} = \begin{bmatrix} 1 & 0 & x_1 & 0 & y_1 & 0 & U_7(S_1, T_1) & U_8(S_1, T_1) \\ 0 & 1 & 0 & x_1 & 0 & y_1 & V_7(S_1, T_1) & V_8(S_1, T_1) \\ 1 & 0 & x_2 & 0 & y_2 & 0 & U_7(S_2, T_2) & U_8(S_2, T_2) \\ 0 & 1 & 0 & x_2 & 0 & y_2 & V_7(S_2, T_2) & V_8(S_2, T_2) \\ 1 & 0 & x_3 & 0 & y_3 & 0 & U_7(S_3, T_3) & U_8(S_3, T_3) \\ 0 & 1 & 0 & x_3 & 0 & y_3 & V_7(S_3, T_3) & V_8(S_3, T_3) \\ 1 & 0 & x_4 & 0 & y_4 & 0 & U_7(S_4, T_4) & U_8(S_4, T_4) \\ 0 & 1 & 0 & x_4 & 0 & y_4 & V_7(S_4, T_4) & V_8(S_4, T_4) \end{bmatrix}. \tag{40}$$

Then,  $\alpha_i$  ( $i = 1-8$ ) can be solved by

$$\boldsymbol{\alpha} = \hat{\mathbf{d}}^{-1} \mathbf{q}^e. \tag{41}$$

It is interesting that, so long as the element nodes are not in coincidence with each other, the matrix  $\hat{\mathbf{d}}$  is hardly singular for various element shapes. Thus, the assumed displacement fields can be rewritten as

$$\hat{\mathbf{u}} = \begin{Bmatrix} \hat{u} \\ \hat{v} \end{Bmatrix} = \mathbf{P}\boldsymbol{\alpha} = \mathbf{P}\hat{\mathbf{d}}^{-1}\mathbf{q}^e. \tag{42}$$

Substitution of Equation (42) into (12) yields the element strains

$$\hat{\boldsymbol{\varepsilon}} = \begin{Bmatrix} \hat{\varepsilon}_x \\ \hat{\varepsilon}_y \\ \hat{\gamma}_{xy} \end{Bmatrix} = \tilde{\mathbf{P}}\hat{\mathbf{d}}^{-1}\mathbf{q}^e = \hat{\mathbf{B}}\mathbf{q}^e, \tag{43}$$

where  $\hat{\mathbf{B}} = \tilde{\mathbf{P}}\hat{\mathbf{d}}^{-1}$  is the strain-displacement matrix, and

$$\tilde{\mathbf{P}} = \begin{bmatrix} 0 & 0 & 1 & 0 & 0 & 0 & \varepsilon_{x7} & \varepsilon_{x8} \\ 0 & 0 & 0 & 0 & 0 & 1 & \varepsilon_{y7} & \varepsilon_{y8} \\ 0 & 0 & 0 & 1 & 1 & 0 & \gamma_{xy7} & \gamma_{xy8} \end{bmatrix}, \tag{44}$$

in which  $\varepsilon_{xi}, \varepsilon_{yi}$ , and  $\gamma_{xyi} (i = 7, 8)$  are the strain solutions derived from  $\phi_7 = S^3$  and  $\phi_8 = T^3$ , respectively.  $\varepsilon_{x7}, \varepsilon_{y7}$ , and  $\gamma_{xy7}$  are given in Equation (17) or (20), and  $\varepsilon_{x8}, \varepsilon_{y8}$ , and  $\gamma_{xy8}$  are given in Equation (23) or (26).

Then, according to the constitutive relations, the corresponding stresses can be obtained

$$\hat{\boldsymbol{\sigma}} = \begin{Bmatrix} \hat{\sigma}_x \\ \hat{\sigma}_y \\ \hat{\tau}_{xy} \end{Bmatrix} = \mathbf{D}\hat{\boldsymbol{\varepsilon}} = \mathbf{D}\hat{\mathbf{B}}\mathbf{q}^e = \mathbf{D}\tilde{\mathbf{P}}\hat{\mathbf{d}}^{-1}\mathbf{q}^e = \hat{\mathbf{P}}\hat{\mathbf{d}}^{-1}\mathbf{q}^e = \hat{\mathbf{S}}\mathbf{q}^e, \tag{45}$$

where  $\mathbf{D}$  is the elasticity matrix,

$$\mathbf{D} = \begin{bmatrix} \hat{D}_{11} & \hat{D}_{12} & \hat{D}_{16} \\ \hat{D}_{21} & \hat{D}_{22} & \hat{D}_{26} \\ \hat{D}_{61} & \hat{D}_{62} & \hat{D}_{66} \end{bmatrix} = \mathbf{C}^{-1} = \begin{bmatrix} \hat{C}_{11} & \hat{C}_{12} & \hat{C}_{16} \\ \hat{C}_{21} & \hat{C}_{22} & \hat{C}_{26} \\ \hat{C}_{61} & \hat{C}_{62} & \hat{C}_{66} \end{bmatrix}^{-1}, \tag{46}$$

in which  $\hat{D}_{ij} (i, j = 1, 2, 6)$  are the reduced elastic moduli;  $\hat{\mathbf{S}} = \hat{\mathbf{P}}\hat{\mathbf{d}}^{-1}$  is the stress matrix; and

$$\hat{\mathbf{P}} = \begin{bmatrix} 0 & 0 & \hat{D}_{11} & \hat{D}_{16} & \hat{D}_{16} & \hat{D}_{12} & \sigma_{x7} & \sigma_{x8} \\ 0 & 0 & \hat{D}_{21} & \hat{D}_{26} & \hat{D}_{26} & \hat{D}_{22} & \sigma_{y7} & \sigma_{y8} \\ 0 & 0 & \hat{D}_{61} & \hat{D}_{66} & \hat{D}_{66} & \hat{D}_{62} & \tau_{xy7} & \tau_{xy8} \end{bmatrix}, \tag{47}$$

$\sigma_{xi}, \sigma_{yi}$ , and  $\tau_{xyi} (i = 7, 8)$  are the stress solutions derived from  $\phi_7 = S^3$  and  $\phi_8 = T^3$ , respectively.  $\sigma_{x7}, \sigma_{y7}$ , and  $\tau_{xy7}$  are given in Equation (19) (same as in Equation (16));  $\sigma_{x8}, \sigma_{y8}$ , and  $\tau_{xy8}$  are given in Equation (25) (same as in Equation (22)). For isotropic case,  $\hat{\mathbf{P}}$  can be rewritten as follows:

$$\hat{\mathbf{P}} = \begin{bmatrix} 0 & 0 & \frac{E'}{1-\mu'^2} & 0 & 0 & \frac{\mu'E'}{1-\mu'^2} & \sigma_{x7} & \sigma_{x8} \\ 0 & 0 & \frac{\mu'E'}{1-\mu'^2} & 0 & 0 & \frac{E'}{1-\mu'^2} & \sigma_{y7} & \sigma_{y8} \\ 0 & 0 & 0 & \frac{E'}{2(1+\mu')} & \frac{E'}{2(1+\mu')} & 0 & \tau_{xy7} & \tau_{xy8} \end{bmatrix}. \tag{48}$$

Based on the virtual work principle [46], the final element stiffness matrix can be written as [46, 47, 53]

$$\begin{aligned}
 \mathbf{K}^e &= \iint_{A^e} \bar{\mathbf{B}}^T \mathbf{D} \hat{\mathbf{B}} t dA = \int_{-1}^1 \int_{-1}^1 \frac{\bar{\mathbf{B}}^{*T}}{|\mathbf{J}|} \mathbf{D} \hat{\mathbf{B}} |\mathbf{J}| t d\xi d\eta \\
 &= \int_{-1}^1 \int_{-1}^1 \bar{\mathbf{B}}^{*T} \mathbf{D} \hat{\mathbf{B}} t d\xi d\eta = \int_{-1}^1 \int_{-1}^1 \bar{\mathbf{B}}^{*T} \hat{\mathbf{S}} t d\xi d\eta, \\
 &= \int_{-1}^1 \int_{-1}^1 \bar{\mathbf{B}}^{*T} \hat{\mathbf{P}} \hat{\mathbf{d}}^{-1} t d\xi d\eta
 \end{aligned} \tag{49}$$

where  $t$  is the thickness of element, and all formulations can be expressed in terms of isoparametric coordinates  $\xi$  and  $\eta$  by using Equations (7) and (36). Furthermore, it can be seen that there is no Jacobian determinant existing Equation (49). The full integration scheme for evaluating Equation (49) is  $2 \times 2$ . The detailed derivation of Equation (49) is given in the appendix.

The equivalent nodal load vector is determined by the same procedure for the isoparametric bilinear element Q4. And the stress results at any point can be directly evaluated by substituting the isoparametric, or Cartesian, or even area coordinates of this point within an element into Equation (45).

This new model is denoted as US-ATFQ4.

#### 4. NUMERICAL EXAMPLES

In this section, the performance of the new element US-ATFQ4 will be fully tested by almost all severe benchmark problems that can be found in literatures. The computer program with double precision for element US-ATFQ4 was compiled by using Fortran90 language and executed under Microsoft Visual Studio 2008 platform. And results solved by other 30 4-node quadrilateral elements listed in Table I are also given for comparison.

##### 4.1. Constant stress/strain problems ( $C_0$ patch test)

*Example 4.1.1 Conventional constant stress/strain patch test using extremely distorted meshes (Figure 5).* As shown in Figure 5, three meshes are used to compute a plane stress patch under constant stress/strain state. Some elements in Meshes B and C are so distorted that their shapes have degenerated into triangles and concave quadrangles, respectively. The displacement fields corresponding to the constant strain are

$$u = 10^{-3}(x + y/2), \quad v = 10^{-3}(y + x/2). \tag{50}$$

And the corresponding exact stress solutions are

$$\sigma_x = \sigma_y = 1333.3333, \quad \tau_{xy} = 400.0. \tag{51}$$

The displacements, obtained in Equation (50), of the boundary nodes are imposed as the displacement boundary conditions. Table II shows the results presented by the new element US-ATFQ4. It can be observed that, no matter the shapes of the elements are convex or concave, the exact results of the displacements and the stresses at each node can be obtained. In fact, the exact stresses at any point (by substituting the Cartesian coordinates into Equation (45)) can also be obtained. It is undoubted that the element US-ATFQ4 can strictly pass this test, even with the extremely distorted shapes.

Elements Q6 [4], AGQ6-I [31], AGQ6-II [31], QACII6 [29], QAC-ATF4 [35], and QACIII6 [30] cannot pass this patch test.

Table I. List of element models for comparison.

Number	Symbol	Elements for comparison	References
1	Q4	Conventional 4-node isoparametric element	[3] MacNeal and Harder
2	QUAD4	4-node shell element in MSC/NASTRAN	[4] Wilson <i>et al.</i>
3	Q6	4-node incompatible isoparametric element	[5] Taylor <i>et al.</i>
4	QM6	4-node incompatible isoparametric element	[6] Cook
5	HL	4-node incompatible isoparametric element	[6] Abaqus element
6	CPS4/CPE4I	4-node incompatible element with assumed strains	[6] Abaqus element
7	CPE4H	4-node hybrid element for plane strain problem	[8] Pian and Sumihara
8	P-S	4-node hybrid stress element	[9] Wu <i>et al.</i>
9	NQ6	4-node incompatible hybrid stress element	[10] Pian and Wu
10	NQ10	4-node incompatible hybrid stress element	[12] Sze
11	SPS	4-node hybrid stress elements with adjustable parameters	[12] Sze
12	SYHP	4-node hybrid stress elements with adjustable parameters	[13] Cen <i>et al.</i>
13	HH4-3 $\beta$	4-node hybrid stress element based on Hamilton principle	[14] Long <i>et al.</i>
14	GC-Q6	4-node generalized conforming element	[15] Chen and Tang
15	QC6	4-node quasi-conforming element	[16] Piltner and Taylor
16	QE2	4-node assumed strain element	[19] Piltner and Taylor
17	B-QE4	4-node assumed strain element (B-bar)	[62] Andelfinger and Ramm
18	PEAS7	4-node assumed strain element	[31] Chen <i>et al.</i>
19	AGQ6-I	4-node incompatible element using QACM-I	[31] Chen <i>et al.</i>
20	AGQ6-II	4-node incompatible element using QACM-I	[32] Cen <i>et al.</i>
21	QACM4	4-node incompatible element using QACM-I	[29] Cen <i>et al.</i>
22	QACII6	4-node incompatible element using QACM-II	[35] Cen <i>et al.</i>
23	QAC-ATF4	4-node element with analytical trial functions using QACM-II	[30] Long <i>et al.</i>
24	QACIII6	4-node incompatible element using QACM-III	[30] Long <i>et al.</i>
25	CQAC6	4-node incompatible element using QACM-I and III	[30] Long <i>et al.</i>
26	F-M QUAD4-P	'FE-meshfree' 4-node element with polynomial basis functions	[20] Rejendran and Zhang
27	F-M QUAD4-R	'FE-meshfree' 4-node element with radial basis functions	[21] Xu and Rejendran
28	Q4S	4-node element with drilling DOFs	[63] MacNeal and Harder
29	D-type	4-node element with drilling DOFs	[64] Ibrahimgovic <i>et al.</i>
30	HSF-Q4 $\theta$ - 7 $\beta$	4-node hybrid stress-function element with drilling DOFs	[57] Cen <i>et al.</i>

MSC/NASTRAN, MacNeal-Schwendler Corporation/National Aeronautics and Space Administration structure analysis; QACM, quadrilateral area coordinate method.

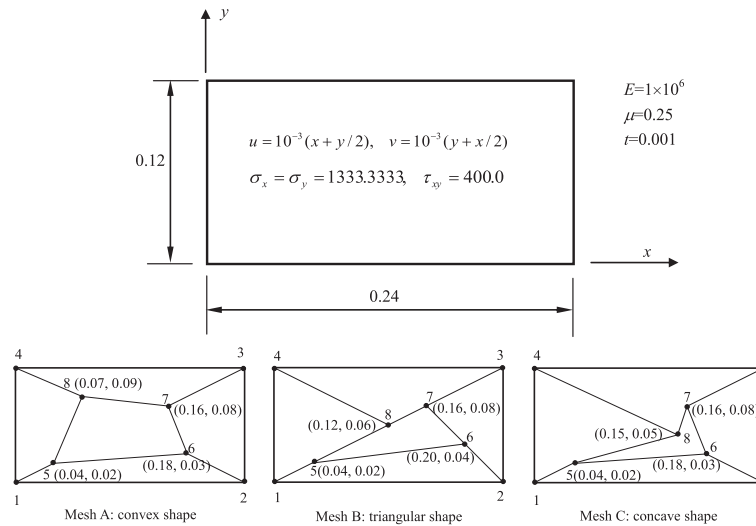


Figure 5. Conventional constant strain/stress patch test.

Table II. Results of US-ATFQ4 for the conventional constant stress/strain patch test (Figure 5).

Mesh	Node	Cartesian coordinate		Result (exact solution)				
		$x$	$y$	$u$	$v$	$\sigma_x$	$\sigma_y$	$\tau_{xy}$
Mesh A convex	5	0.04	0.02	$0.500 \times 10^{-4}$	$0.400 \times 10^{-4}$	1333.333	1333.333	400.0
	6	0.18	0.03	$0.195 \times 10^{-3}$	$0.120 \times 10^{-3}$	1333.333	1333.333	400.0
	7	0.16	0.08	$0.200 \times 10^{-3}$	$0.160 \times 10^{-3}$	1333.333	1333.333	400.0
	8	0.07	0.09	$0.115 \times 10^{-3}$	$0.125 \times 10^{-3}$	1333.333	1333.333	400.0
Mesh B triangular	5	0.04	0.02	$0.500 \times 10^{-4}$	$0.400 \times 10^{-4}$	1333.333	1333.333	400.0
	6	0.20	0.04	$0.220 \times 10^{-3}$	$0.140 \times 10^{-3}$	1333.333	1333.333	400.0
	7	0.16	0.08	$0.200 \times 10^{-3}$	$0.160 \times 10^{-3}$	1333.333	1333.333	400.0
	8	0.12	0.06	$0.150 \times 10^{-3}$	$0.120 \times 10^{-3}$	1333.333	1333.333	400.0
Mesh C concave	5	0.04	0.02	$0.500 \times 10^{-4}$	$0.400 \times 10^{-4}$	1333.333	1333.333	400.0
	6	0.18	0.03	$0.195 \times 10^{-3}$	$0.120 \times 10^{-3}$	1333.333	1333.333	400.0
	7	0.16	0.08	$0.200 \times 10^{-3}$	$0.160 \times 10^{-3}$	1333.333	1333.333	400.0
	8	0.15	0.05	$0.175 \times 10^{-3}$	$0.125 \times 10^{-3}$	1333.333	1333.333	400.0

Example 4.1.2 The constant stress/strain strong patch test (Figure 6). Figure 6 shows a two element patch test (plane stress state) with axial loads applied at the free end of a cantilever beam. All geometric and material parameters are also given in Figure 6. The distortion parameter  $e$  can be used to move from a rectangular division to a highly distorted mesh division. The exact solutions for stresses are  $\sigma_x = 0.5, \sigma_y = 0$ , and  $\tau_{xy} = 0$ . And the exact axial displacement at the loaded end, that is, nodes A and B, should be  $u = 0.06667$ .

The new element US-ATFQ4 can present exact solutions for both displacements and stresses at any nodes and points. The normalized axial displacement results at nodes A and B with different  $e$  are shown in Table III. It can be seen that element AGQ6-II [31, 43] cannot pass this test.

#### 4.2. Pure bending tests

Example 4.2.1 Cantilever beam divided by two elements containing a parameter of distortion (Figure 7). As shown in Figure 7, a pure bending moment is applied at the free end of a cantilever beam by using a couple. The geometric, material, and mesh conditions for the cantilever beam are

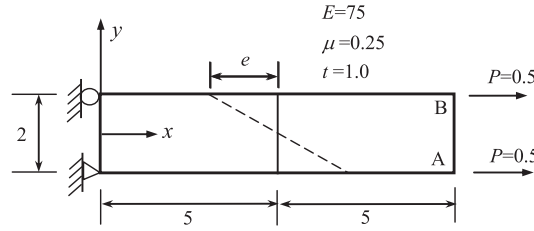


Figure 6. Constant stress/strain strong patch test with two elements.

Table III. Normalized axial displacement results at the free end of a cantilever beam (Figure 6).

$e$	0	0.5	1	2	3	4	4.9
<b>US-ATFQ4</b>	<b>1.000</b>						
AGQ6-I [31, 43]	1.000	—	1.000	1.000	1.000	1.000	—
AGQ6-II [31, 43]	1.000	—	1.054	1.225	1.544	2.084	—

Data in bold are the results obtained by the models proposed in this paper.

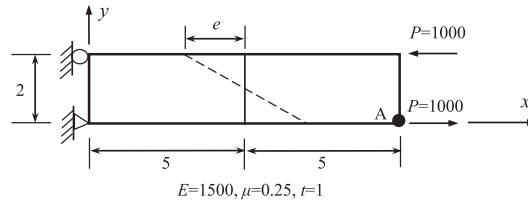


Figure 7. Pure bending patch test with two elements.

also given in Figure 7, in which  $e$  is a parameter of distortion. This is a famous benchmark for testing the sensitivity to the mesh distortion. The exact solutions for stresses and displacements are  $\sigma_x = -3000y + 3000$ ,  $\sigma_y = 0$ ,  $\tau_{xy} = 0$ ,  $u = 2x(1 - y)$ ,  $v = x^2 + 0.25y^2 - 0.5y$ .

When  $e$  varies from 0 to 5 ( $0 \leq e < 0.5$ ), the new element US-ATFQ4 can present exact solutions for both displacements at each node and stresses at any point. Results of the tip deflection  $v_A$  (the exact value is 100) at point A are listed in Table IV. Besides the present element, the solutions obtained by other 19 models are also given for comparison. Among the elements that can pass the  $C_0$  patch test, US-ATFQ4 is the only model that can perfectly pass this pure bending patch test.

*Example 4.2.2 Pure bending for a cantilever beam with different meshes (Figure 8).* Although the new element US-ATFQ4 passes the pure bending patch test given in the last example, it cannot be expected to present exact pure bending solutions for all conditions. This is because the trial functions used in Equation (38) are not complete in quadratic terms of QACM-II.  $(U_7, V_7)$  and  $(U_8, V_8)$  are only corresponding to the pure bending solutions of the stress functions  $\phi = S^3$  and  $\phi = T^3$ , respectively. But the terms corresponding to  $\phi = S^2T$  and  $\phi = ST^2$  are missing. This example [22], which is usually adopted for testing 8-node element, will show the performance of the new element using various meshes for pure bending problem.

As shown in Figure 8, a cantilever beam under plane stress condition is subjected to a constant bending moment  $M$ . The theoretical solutions for this problem are given in [65]

$$\sigma_x = \frac{240}{c}y - 120, \quad \sigma_y = 0, \quad \tau_{xy} = 0; \tag{52}$$

$$u = -\frac{120}{E}x + \frac{240}{cE}xy, \quad v = \frac{36}{E}y - \frac{120}{cE}x^2 - \frac{36}{cE}y^2. \tag{53}$$

Table IV. Results of the tip deflection  $v_A$  of a pure bending cantilever beam with a distorted parameter  $e$  (Figure 7).

$e$		0	0.5	1	2	3	4	4.9
Elements that <b>cannot</b> pass the $C_0$ patch test	Q6 [4]	100	93.21	86.89	92.67	102.42	110.52	116.6
	AGQ6-I [31]	100	100	100	100	100	100	100
	AGQ6-II [31]	100	100	100	100	100	100	100
	QACII6 [29]	100	100	100	100	100	100	100
	QAC-ATF4 [35]	100	100	100	100	100	100	100
	QACIII6 [30]	100	100	100	100	100	100	100
Elements that <b>can</b> pass the $C_0$ patch test	Q4	28.0	21.0	14.1	9.7	8.3	7.2	6.2
	QM6 [5]	100	80.9	62.7	54.4	53.6	51.2	46.8
	P-S [8]	100	81.0	62.9	55.0	54.7	53.1	49.8
	SPS [12]	—	—	110.0	120.5	132.7	147.1	162.6
	SYHP [12]	—	—	110.0	120.5	132.8	147.5	163.3
	CPS4I [6]	100	73.53	56.16	50.31	50.38	49.39	46.58
	QE2 [16]	100	81.2	63.4	56.5	57.5	57.9	56.9
	B-QE4 [19]	100	81.2	63.4	56.5	57.5	57.9	56.9
	QACM4 [32]	100	83.8	66.5	60.1	61.4	60.3	56.0
	CQAC6 [30]	100	83.8	66.5	60.1	61.4	60.3	56.0
	F-M QUAD4-P [20]	9.85	9.94	10.22	11.08	12.00	12.64	12.88
	F-M QUAD4-R [21]	99.28	99.28	99.28	99.28	99.28	99.29	99.29
	HSF-Q4 $\theta$ -7 $\beta$ [57]	100	99.93	99.47	95.95	87.14	71.87	52.47
	<b>US-ATFQ4</b>	<b>100</b>						
Exact	100	100	100	100	100	100	100	

Data in bold are the results obtained by the models proposed in this paper.

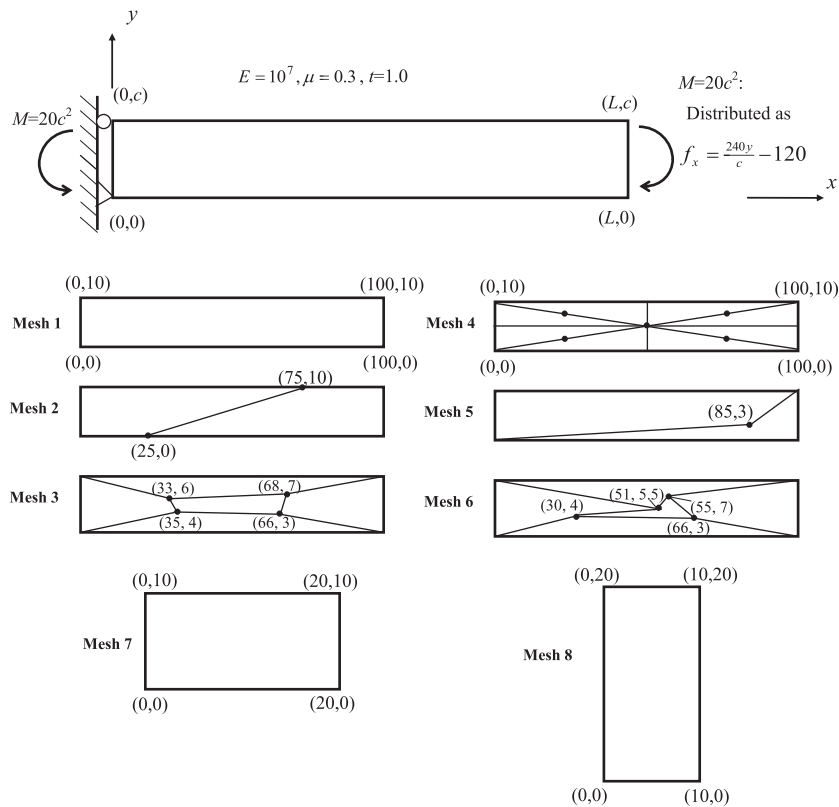


Figure 8. Pure bending problems and meshes for a cantilever beam.

Table V. Results at selected locations for the pure bending problem (Figure 8).

		Q4	CPS4I [6]	US-ATFQ4	Exact
Mesh 1	$\sigma_x(0,10)$	3.3333	120.00	<b>120.00</b>	120.0
	$\sigma_x(0,0)$	-3.3333	-120.00	<b>-120.00</b>	-120.0
	$v(100,0) \times 10^3$	-0.30333	-12.00	<b>-12.00</b>	-12.0
Mesh 2	$\sigma_x(0,10)$	2.2871	59.068	<b>120.00</b>	120.0
	$\sigma_x(0,0)$	-6.8328	-59.068	<b>-120.00</b>	-120.0
	$v(100,0) \times 10^3$	-0.30511	-3.9319	<b>-12.000</b>	-12.0
Mesh 3	$\sigma_x(0+,10)$	2.6056	14.892	<b>119.30</b>	120.0
	$\sigma_x(0,10-)$	0.83967	18.443	<b>120.64</b>	120.0
	$\sigma_x(0,0+)$	-0.84182	-12.225	<b>-118.45</b>	-120.0
	$\sigma_x(0+,0)$	-2.5956	-17.042	<b>-121.10</b>	-120.0
	$v(100,0) \times 10^3$	-0.28193	-1.5813	<b>-11.504</b>	-12.0
Mesh 4	$\sigma_x(0,10)$	5.7019	90.960	<b>103.75</b>	120.0
	$\sigma_x(0,0)$	-5.7019	-90.960	<b>-103.75</b>	-120.0
	$v(100,0) \times 10^3$	-0.72369	-7.6926	<b>-12.695</b>	-12.0
Mesh 5	$\sigma_x(0,10)$			<b>140.31</b>	120.0
	$\sigma_x(0,0)$	Failed	Failed	<b>-96.025</b>	-120.0
	$v(100,0) \times 10^3$			<b>-11.969</b>	-12.0
Mesh 6	$\sigma_x(0+,10)$	2.4060	3.9425	<b>130.04</b>	120.0
	$\sigma_x(0,10-)$	0.33859	-4.9271	<b>118.50</b>	120.0
	$\sigma_x(0,0+)$	-0.13273	-21.167	<b>-126.67</b>	-120.0
	$\sigma_x(0+,0)$	-2.6335	-2.2627	<b>-120.67</b>	-120.0
	$v(100,0) \times 10^3$	-0.26150	-0.41228	<b>-12.056</b>	-12.0
Mesh 7	$\sigma_x(0,10)$	50.000	120.00	<b>120.00</b>	120.0
	$\sigma_x(0,0)$	-50.000	-120.00	<b>-120.00</b>	-120.0
	$v(20,0) \times 10^4$	-1.8200	-4.8000	<b>-4.8000</b>	-4.8
Mesh 8	$\sigma_x(0,20)$	110.34	120.00	<b>120.000</b>	120.0
	$\sigma_x(0,0)$	-110.34	-120.00	<b>-120.000</b>	-120.0
	$v(10,0) \times 10^5$	5.0207	-4.8000	<b>-4.8000</b>	-4.8

Data in bold are the results obtained by the models proposed in this paper.

Eight types of regular and distorted mesh divisions are employed (Figure 8), in which Meshes 4, 5 and 6 are so severely distorted that some quadrilateral elements degenerate into triangles or concave quadrangles.

Results obtained by the new element US-ATFQ4, the isoparametric element Q4, and the incompatible Abaqus element CPS4I [6] are listed in Table V. It can be observed that the present element US-ATFQ4 can provide good solutions even in extremely distorted meshes.

#### 4.3. Bending problems for various rectangular cantilever beams under plane stress state

*Example 4.3.1 Cantilever beam divided by five distorted quadrilateral elements (Figure 9).* A cantilever beam, as shown in Figure 9, is divided by five irregular quadrilateral elements. And two loading cases are considered as follows: (1) pure bending under moment  $M$ ; and (2) linear bending under transverse force  $P$ . Results of the vertical deflection  $v_A$  at point A and the stress  $\sigma_{xB}$  at point B are given in Table VI. It can be observed that, the new element US-ATFQ4 presents not only exact solutions for pure bending case but also high precision results for linear bending case.

*Example 4.3.2 Cantilever beam divided by four distorted quadrilateral elements (Figure 10).* As shown in Figure 10, a cantilever beam with fully fixed end is subjected to a quadratic distributed shear load at its free end, and the beam is divided by four distorted quadrilateral elements. Results of the deflections at the tip points A and B are shown in Table VII. It can be seen that the present

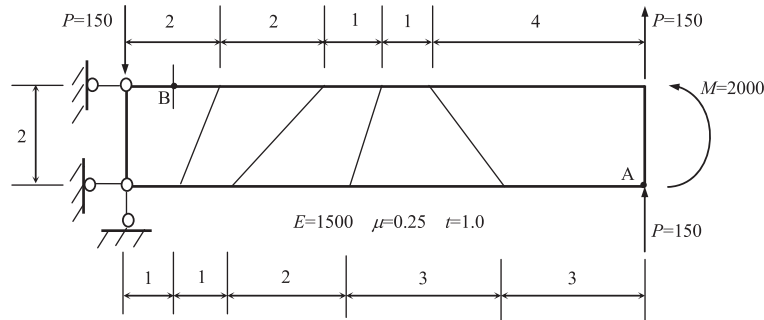


Figure 9. Cantilever beam divided by five distorted elements.

Table VI. The deflections and stresses at selected locations for bending problems of a cantilever beam (Figure 9).

Element model		Load $M$		Load $P$	
		$v_A$	$\sigma_{xB}$	$v_A$	$\sigma_{xB}$
Elements that <b>cannot</b> pass the $C_0$ patch test	Q6 [4]	98.4	-2428	100.4	-3354
	AGQ6-I [31]	100.0	-3000	102.0	-4151
	AGQ6-II [31]	100.0	-3000	102.7	-4180
	QACII6 [29]	100.0	-3000	102.7	-4180
	QAC-ATF4 [35]	100.0	-3000	102.4	-4029
	QACIII6 [30]	100.0	-3000	102.7	-4150
Elements that <b>can</b> pass the $C_0$ patch test	Q4	45.7	-1761	50.7	-2448
	QM6 [5]	96.1	-2497	98.0	-3235
	CPS4I [6]	92.3	-2996	97.0	-3932
	P-S [8]	96.2	-3014	98.2	-4137
	NQ6 [9]	96.1	-2439	98.0	-3294
	NQ10 [10]	96.0	-2986	97.9	-4021
	SPS [12]	101.8	-3003	—	—
	SYHP [12]	101.8	-3002	—	—
	GC-Q6 [14]	95.0	-3036	96.1	-4182
	QC6 [15]	96.1	-2439	98.1	-3339
	QE2 [16]	96.5	-3004	98.3	-3906
	$\tilde{B}$ -QE4 [19]	96.5	-3004	98.3	-3906
	QACM4 [32]	96.0	-3015	98.0	-4135
	CQAC6 [30]	96.0	-3015	98.0	-4135
	<b>US-ATFQ4</b>	<b>100.0</b>	<b>-3000</b>	<b>101.5</b>	<b>-3938</b>
Exact	100.0	-3000	102.6	-4050	

Data in bold are the results obtained by the models proposed in this paper.

element possesses the best precisions, even better than the elements that cannot pass the  $C_0$  patch test, and the elements Q4S [63], D-type [64], and HSF-Q4 $\theta$ -7 $\beta$  [57] with vertex drilling DOFs (the total DOF number of the elements Q4S, D-type, and HSF-Q4 $\theta$ -7 $\beta$  is 12 because of the additional vertex drilling DOFs).

*Example 4.3.3 MacNeal's thin cantilever beam with distorted meshes (Figure 1).* This example has been described in Section 1. It is a famous benchmark [3] for testing the sensitivity to mesh distortion of the 4-node quadrilateral membrane elements. Consider the thin beams given in Figure 1. Three different mesh shapes are adopted: rectangle, parallelogram, and trapezoid. Besides the distortion caused by the length-width ratio, the composite distortions of parallelogram and trapezoidal shapes together with length-width ratio are also taken into account. Two loading cases are considered: pure bending  $M$  and transverse linear bending  $P$  (Figure 1). The results of the tip deflection are shown

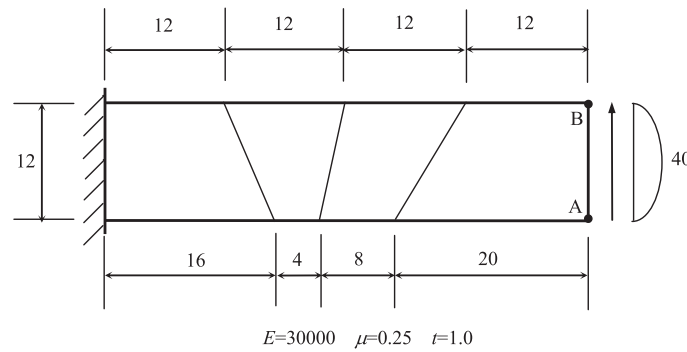


Figure 10. Cantilever beam divided by four distorted elements.

Table VII. The deflections at selected locations for bending problem of a cantilever beam (Figure 10).

Element	Tip deflection			Normalized value		
	Point A	Point B	Average	Point A	Point B	Average
Q4	0.2126	0.2131	0.2129	0.598	0.599	0.598
QM6 [5]	0.3264	0.3286	0.3275	0.917	0.924	0.920
CPS4I [6]	0.3291	0.3315	0.3303	0.925	0.932	0.928
QACM4 [32]	0.3280	0.3305	0.3293	0.922	0.929	0.926
CQAC6 [30]	0.3280	0.3305	0.3293	0.922	0.929	0.926
AGQ6-I [31]	0.3510	0.3509	0.3510	0.987	0.986	0.987
AGQ6-II [31]	0.3535	0.3530	0.3533	0.994	0.992	0.993
QACII6 [29]	0.3535	0.3530	0.3533	0.994	0.992	0.993
QAC-ATF4 [35]	0.3523	0.3516	0.3520	0.990	0.988	0.989
QACIII6 [30]	0.3535	0.3530	0.3533	0.994	0.992	0.993
Q4S [63]	—	—	0.2978	—	—	0.837
D-type [64]	—	—	0.3065	—	—	0.861
HSF-Q4θ-7β [57]	0.3506	0.3469	0.3486	0.985	0.975	0.980
<b>US-ATFQ4</b>	<b>0.3545</b>	<b>0.3544</b>	<b>0.3544</b>	<b>0.996</b>	<b>0.996</b>	<b>0.996</b>
Reference value	0.3558		1.000			

Data in bold are the results obtained by the models proposed in this paper.

in Table VIII. It is obvious that the present element US-ATFQ4 is free of trapezoidal locking and insensitive to mesh distortion, although it is a model that can strictly pass the  $C_0$  patch test.

#### 4.4. Rotational frame dependence tests

*Example 4.4.1 Rotational frame dependence test on a cantilever beam under pure bending state (Figure 11).* The geometric, material, and load conditions for a pure bending cantilever beam are given in Figure 11. This beam is divided by two distorted elements with six nodes. Let the Cartesian coordinate system  $xoy$  rotate clockwise from  $\alpha = 0^\circ$  to  $90^\circ$  in steps of  $10^\circ$ , the stresses are solved at each step. The exact stress solutions for pure bending state in each new coordinate system  $x'oy'$  are

$$\text{for nodes 1, 2, and 3 : } \sigma_{x'} = 1.5 \cos^2 \alpha, \quad \sigma_{y'} = 1.5 \sin^2 \alpha, \quad \tau_{x'y'} = 1.5 \sin \alpha \cos \alpha; \quad (54)$$

$$\text{for nodes 4, 5, and 6 : } \sigma_{x'} = -1.5 \cos^2 \alpha, \quad \sigma_{y'} = -1.5 \sin^2 \alpha, \quad \tau_{x'y'} = -1.5 \sin \alpha \cos \alpha. \quad (55)$$

Table IX shows the stress results obtained by the present element US-ATFQ4. It can be clearly seen that US-ATFQ4 can provide exact pure bending solutions in all directions. This success indicates that the hypothesis given in Section 2.2 is correct, that is, the linear combination  $\phi = a''T^3 + b''S^3$  (in which  $a''$  and  $b''$  are two undetermined coefficients) may reflect exact solutions for pure bending in all directions.



*Example 4.4.2 Rotational frame dependence test on a cantilever beam with fully fixed end (Figure 12).* The approach of Spilker *et al.* [66] is considered. As shown in Figure 12, a cantilever beam is rotated counterclockwise from 0° to 90° in steps of 10°, and the problem is solved for the displacements at each step. The magnitude of displacement, that is,  $\sqrt{u^2 + v^2}$  at point A is monitored to study the rotational frame-dependent behavior. The mesh used in this test is also given in Figure 12.

Table X shows the results obtained by the present element US-ATFQ4. The magnitude of displacements based on an ‘overkill’ solution obtained using 20,000 8-node quadrilateral elements of Abaqus [6] is used as a reference solution. It can be seen that the present model US-ATFQ4 provides the invariance for the coordinate rotation.

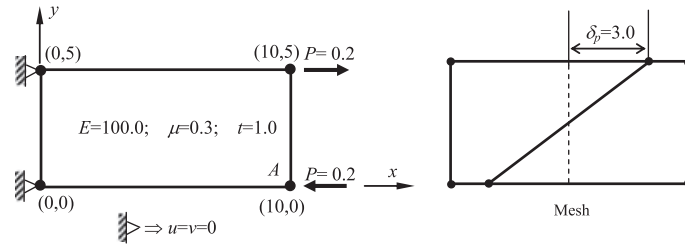


Figure 12. Rotation dependence test: cantilever beam problem and mesh.

Table X. Results of the displacement at point A computed for the rotational frame invariance test (Figure 12).

$\theta$	$u_A$	$v_A$	$\sqrt{u_A^2 + v_A^2}$	Normalized	Percentage error
0°	-2.40000E-02	-4.80000E-02	0.05367	0.9938	-0.6192%
10°	-1.53003E-02	-5.14383E-02	0.05367	0.9938	-0.6192%
20°	-0.61357E-02	-5.33137E-02	0.05367	0.9938	-0.6192%
30°	0.32154E-02	-5.35692E-02	0.05367	0.9938	-0.6192%
40°	1.24687E-02	-5.21970E-02	0.05367	0.9938	-0.6192%
50°	2.13432E-02	-4.92389E-02	0.05367	0.9938	-0.6192%
60°	2.95692E-02	-4.47846E-02	0.05367	0.9938	-0.6192%
70°	3.68968E-02	-3.89696E-02	0.05367	0.9938	-0.6192%
80°	4.31032E-02	-3.19705E-02	0.05367	0.9938	-0.6192%
90°	4.80000E-02	-2.40000E-02	0.05367	0.9938	-0.6192%
Overkill solution	—	—	0.05400	1.0000	0.0000

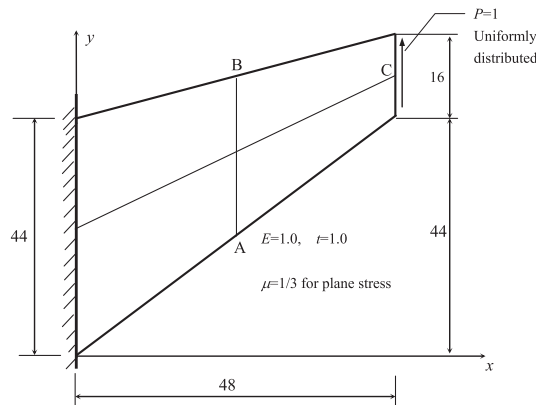


Figure 13. Cook's skew beam problem.

Table XI. Results of Cook's skew beam under plane stress condition (Figure 13).

Elements	$\nu_C$				$\sigma_{Amax}$				$\sigma_{Bmin}$			
	2 × 2	4 × 4	8 × 8	16 × 16	2 × 2	4 × 4	8 × 8	16 × 16	2 × 2	4 × 4	8 × 8	16 × 16
Q4	11.80	18.29	22.08	23.43	0.1217	0.1873	0.2242	0.2311	-0.0960	-0.1524	-0.1869	-0.1966
QM6 [5]	21.05	23.02	—	23.88	0.1928	0.2243	—	0.2364	-0.1580	-0.1856	—	-0.2025
CPS4I [6]	21.05	23.02	23.69	23.88	0.1703	0.2217	0.2342	0.2364	-0.1658	-0.1849	-0.1986	-0.2025
P-S [8]	21.13	23.02	23.69	23.88	0.1854	0.2241	0.2345	0.2364	-0.1550	-0.1856	-0.1986	-0.2025
HH4-3 $\beta$ [13]	22.08	23.44	23.78	23.91	0.0680	0.1533	0.2027	0.2209	-0.1433	-0.1596	-0.1865	-0.1964
QE2 [16]	21.35	23.04	—	23.88	0.1956	0.2261	—	0.2364	-0.1448	-0.1859	—	-0.2025
B-QE4 [19]	21.35	23.04	—	23.88	0.1956	0.2261	—	0.2364	—	—	—	—
QACM4 [32]	20.74	22.99	23.69	—	0.1936	0.2256	0.2345	—	-0.1452	-0.1866	-0.1987	—
HL [61]	18.17	22.03	23.39	—	0.1582	0.1980	—	—	-0.1335	-0.1770	—	—
Q6 [4]	22.94	23.48	23.80	23.91	0.2029	0.2258	0.2334	0.2361	-0.1734	-0.1915	-0.1997	-0.2028
AGQ6-I [31]	23.07	23.68	23.87	—	0.2023	0.2275	0.2351	—	-0.1758	-0.1972	-0.2016	—
AGQ6-II [31]	25.92	24.37	24.04	—	0.2169	0.2286	0.2352	—	-0.1999	-0.2014	-0.2027	—
QACII6 [29]	25.92	24.37	24.04	23.97	0.2169	0.2286	0.2352	0.2365	-0.1999	-0.2014	-0.2027	-0.2035
QAC-ATF4 [35]	24.36	23.84	23.89	—	0.2127	0.2277	0.2350	—	-0.1809	-0.1934	-0.2001	—
F-M QUAD4-P [20]	21.57	23.57	23.86	23.92	0.1860	0.2319	0.2370	0.2370	-0.2183	-0.2101	-0.1999	-0.2033
F-M QUAD4-R [21]	20.40	23.19	23.76	23.89	—	—	—	—	—	—	—	—
HSF-Q4 $\theta$ -7 $\beta$ [57]	22.55	23.44	23.79	23.90	0.2158	0.2357	0.2364	0.2367	-0.2086	-0.2029	-0.2027	-0.2039
<b>US-ATFQ4</b>	<b>22.76</b>	<b>23.43</b>	<b>23.79</b>	<b>23.91</b>	<b>0.1956</b>	<b>0.2252</b>	<b>0.2342</b>	<b>0.2363</b>	<b>-0.1552</b>	<b>-0.1869</b>	<b>-0.1988</b>	<b>-0.2026</b>
Reference solution*		23.9652				0.236880				-0.203524		

Data in bold are the results obtained by the models proposed in this paper.  
 \*Results of the 8-node element using 100 × 100 mesh in Abaqus [6].

4.5. Bending problems for skew beam, curving beam, and wedge

*Example 4.5.1 Cook's skew beam problem (Figure 13).* As shown in Figure 13, a skew cantilever under plane stress condition is subjected to a shear distributed load at the free edge. This example was proposed by Cook *et al.* [67]. The results of vertical deflection at point C, the maximum principal stress at point A, and the minimum principal stress at point B are all listed in Table XI. The present element US-ATFQ4 exhibits very good convergence.

*Example 4.5.2 Bending of a thick curving beam (Figure 14).* As shown in Figure 14, a thick curving cantilever beam meshed into four elements is subjected to a transverse force at its tip. The results of the vertical tip deflection at point A are shown in Table XII. Better solutions can be obtained by the proposed elements than those by other models that can pass the  $C_0$  patch test.

*Example 4.5.3 Bending of a thin curving beam (Figure 15).* As shown in Figure 15, a thin curving cantilever beam is subjected to a transverse force  $P$  at the tip, and it is meshed into five elements. The Poisson ratio is  $\mu = 0.0$ . Two ratios of thickness-radius, (1)  $h/R = 0.03 (E = 365,010.0)$  and (2)  $h/R = 0.006 (E = 4,4027,109.0)$ , are considered. The results of the tip displacement are listed in Table XIII.

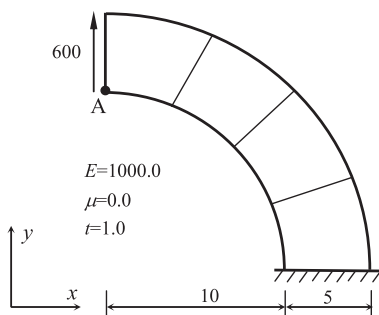


Figure 14. Bending of a thick curving beam.

Table XII. The tip deflection of a thick curving beam (Figure 14).

Element	Q4	QM6 [5]	P-S [8]	CPS4I [6]	PEAS7 [62]	QACM4 [32]	<b>US-ATFQ4</b>	Exact solution
$v_A$	57.9	83.6	84.6	84.6	84.6	84.6	<b>86.3</b>	90.1

Data in bold are the results obtained by the models proposed in this paper.

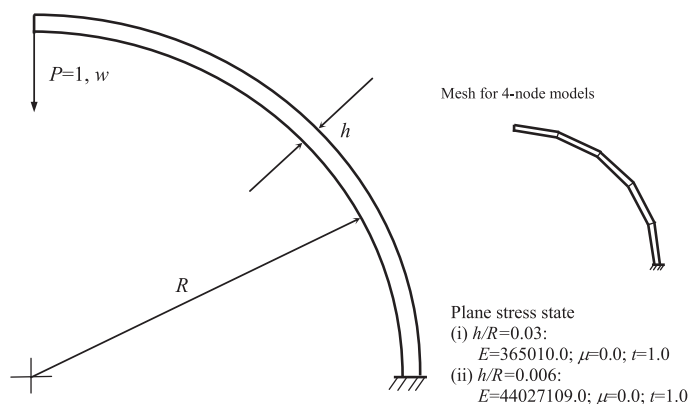


Figure 15. Bending of a thin curving beam.

Compared with the mesh used in the previous example, the shape of the elements in this example becomes much narrower. The length-width ratio of the elements reaches 10 when  $h/R = 0.03$  and will be larger if  $h/R = 0.006$ , and each of the elements is a trapezoid, so the distortion becomes much more serious. From Table XIII, it can be observed that isoparametric elements Q4, Q6, QM6, and QUAD4 are very sensitive to the mesh distortion caused by the increase of the length-width ratio and even locked under the case of  $h/R = 0.006$ , while the new element US-ATFQ4 is insensitive to this kind of distortion and presents the best result.

*Example 4.5.4 A wedge subjected to a uniformly distributed load (Figure 16).* As shown in Figure 16, a cantilever wedge is subjected to a uniformly distributed load  $q$ . Because of its triangular shape, the wedge cannot be modeled without the use of triangular and/or distorted quadrilateral elements. The theoretical solutions for this problem are given in [65]

$$\left. \begin{aligned} \sigma_r &= \frac{q}{\operatorname{tg}\alpha - \alpha} (\alpha - \theta - \sin\theta \cos\theta - \sin^2\theta \operatorname{tg}\alpha) \\ \sigma_\theta &= \frac{q}{\operatorname{tg}\alpha - \alpha} (\alpha - \theta + \sin\theta \cos\theta - \cos^2\theta \operatorname{tg}\alpha) \\ \tau_{r\theta} &= \frac{q}{2(\operatorname{tg}\alpha - \alpha)} (1 + \sin^2\theta - \cos^2\theta - 2\operatorname{tg}\alpha \sin\theta \cos\theta) \end{aligned} \right\}. \quad (56)$$

Because the present quadrilateral element US-ATFQ4 can still perform well when its shape degenerates into triangle, it can therefore be readily used to model the wedge problem. As shown in Figure 16, three mesh divisions,  $1 \times 6$ ,  $2 \times 12$ , and  $4 \times 24$ , are employed, in which some elements

Table XIII. The tip deflection of a thin curving beam (Figure 15).

$h/R$	Q4	QUAD4 [3]	Q6 [4]	QM6 [5]	CPS4I [6]	QACM4 [32]	<b>US-ATFQ4</b>	Exact solution
0.03	0.016	0.615	0.770	0.339	0.650	0.639	<b>0.987</b>	1.000
0.006	0.001	0.163	0.285	0.022	0.173	0.026	<b>0.987</b>	1.000

Data in bold are the results obtained by the models proposed in this paper.

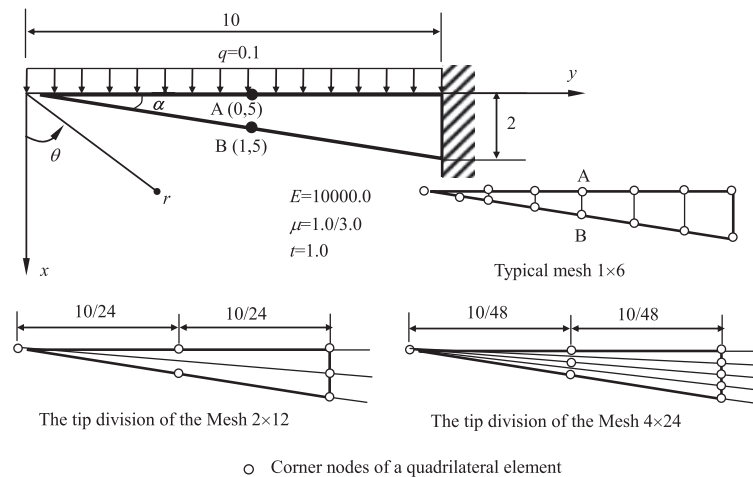


Figure 16. A wedge subjected to a uniformly distributed load.

Table XIV. US-ATFQ4 results of radial stress at selected points for a wedge subjected to a uniformly distributed load (Figure 16).

Mesh	$1 \times 6$	$2 \times 12$	$4 \times 24$	Exact [65]
$\sigma_r$ at point A (0, 5)	7.7143 (1.78%)	7.5813 (0.03%)	7.5821 (0.04%)	7.5792
$\sigma_r$ at point B (1, 5)	-7.9241 (3.19%)	-7.7430 (0.83%)	-7.6883 (0.12%)	-7.6792

Table XV. Tip deflection for MacNeal's thin beam under plane strain condition (Figure 1).

Mesh	Element	Load P					Load M				
		$\mu = 0.49$	$\mu = 0.499$	$\mu = 0.4999$	$\mu = 0.49999$	$\mu = 0.499999$	$\mu = 0.49$	$\mu = 0.499$	$\mu = 0.4999$	$\mu = 0.49999$	$\mu = 0.499999$
Mesh (a)	Q4	-0.004295	-0.000701	-0.000154	-0.000096	-0.0000212	-0.000031	-0.000003	-0.000000		
	CPE4H [6]	-0.012382	-0.012457	-0.012464	-0.012465	-0.000619	-0.000623	-0.000623	-0.000623		
	CPE4I [6]	-0.081589	-0.080635	-0.080538	-0.080529	-0.004104	-0.004055	-0.004051	-0.004050		
	F-M QUAD4-P [20]	-0.061586	-0.059221	-0.027486	-0.004104	-0.004100	-0.003942	-0.001830	-0.002726		
	<b>US-ATFQ4</b>	<b>-0.081589</b>	<b>-0.080635</b>	<b>-0.080538</b>	<b>-0.080529</b>	<b>-0.004103</b>	<b>-0.004055</b>	<b>-0.004051</b>	<b>-0.004050</b>		
Mesh (b)	Q4	-0.001247	-0.000430	-0.000166	-0.000116	-0.000045	-0.000014	-0.000004	-0.000001		
	CPE4H [6]	-0.006257	-0.006287	-0.006290	-0.006290	-0.000305	-0.000307	-0.000307	-0.000307		
	CPE4I [6]	-0.052100	-0.051499	-0.051438	-0.051432	-0.002981	-0.002946	-0.002943	-0.002943		
	F-M QUAD4-P [20]	-0.059599	-0.040129	-0.005372	-0.000994	-0.003969	-0.002673	-0.000356	-0.000067		
	<b>US-ATFQ4</b>	<b>-0.081314</b>	<b>-0.080353</b>	<b>-0.080255</b>	<b>-0.080246</b>	<b>-0.004103</b>	<b>-0.004055</b>	<b>-0.004051</b>	<b>-0.004050</b>		
Mesh (c)	Q4	-0.001736	-0.001026	-0.000765	-0.000715	-0.000074	-0.000050	-0.000039	-0.000037		
	CPE4H [6]	-0.003210	-0.003209	-0.003209	-0.003209	-0.000127	-0.000127	-0.000127	-0.000127		
	CPE4I [6]	-0.004398	-0.004354	-0.004350	-0.004349	-0.000201	-0.000199	-0.000198	-0.000198		
	F-M QUAD4-P [20]	-0.061224	-0.046108	-0.013397	-0.002428	-0.004076	-0.003070	-0.000890	-0.000162		
	<b>US-ATFQ4</b>	<b>-0.080284</b>	<b>-0.079200</b>	<b>-0.079089</b>	<b>-0.079078</b>	<b>-0.004103</b>	<b>-0.004055</b>	<b>-0.004051</b>	<b>-0.004050</b>		
Reference solutions		-0.082170	-0.081209	-0.081112	-0.081102	-0.004103	-0.004055	-0.004051	-0.004050		

Data in bold are the results obtained by the models proposed in this paper.

are triangular in shape. Numerical results and the percentage errors of the radial stresses at selected points are listed in Tables XIV. Again, the present element US-ATFQ4 performs very well for such high-order bending problem.

#### 4.6. Nearly incompressible problems

*Example 4.6.1 MacNeal's thin beam under plane strain condition (Figure 1).* The MacNeal's thin beam problem given in Example 4.3.3 is considered again. The tip deflection is re-computed under plain strain condition by varying the Poisson's ratio as  $\mu = 0.49, 0.499, 0.4999, \text{ and } 0.49999$ . Results obtained by the present element and some other models are summarized in Table XV. The exact solutions for pure and linear bending states are taken as the reference solutions. It can be seen that the new element US-ATFQ4 is the only model that is free of the volumetric locking in all meshes.

*Example 4.6.2 Thick-walled cylinder (Figure 17).* A thick-walled cylinder under plane strain condition is subjected to a uniformly distributed internal pressure  $p = 1$ . Because of symmetry, only a quarter of the cylinder is considered, as shown in Figure 17. The exact solution of the radial displacement  $u_r$  is given in

$$u_r = \frac{(1 + \mu)pR_1^2}{E(R_2^2 - R_1^2)} [R_2^2/r + (1 - 2\mu)r], \quad (57)$$

where  $R_1$  is the inner radius and  $R_2$  is the outer radius. In this example, let  $R_1 = 3, R_2 = 9$ . So, when the Poisson's ratio  $\mu = 0.49, 0.499, 0.4999$ , the corresponding radial displacement  $u_r$  at  $r = R_1$  are  $5.0399 \times 10^{-3}, 5.0602 \times 10^{-3}, 5.0623 \times 10^{-3}$ , respectively.

Table XVI shows the normalized results of the radial displacement  $u_r$  at  $r = R_1$ . It can be seen again that the present element US-ATFQ4 is free of the volumetric locking.

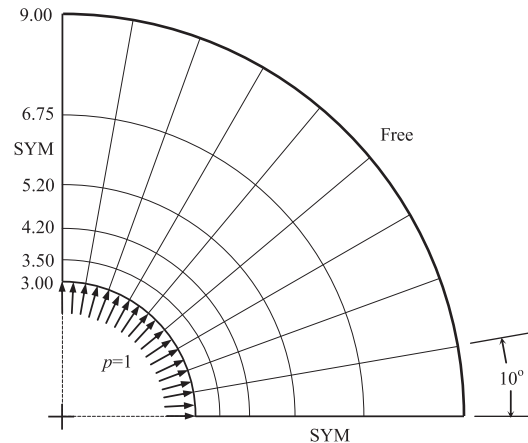


Figure 17. Thick-walled cylinder. Inner radius = 3.0; outer radius = 9.0; thickness = 1.0;  $E = 1000$ ;  $\mu = 0.49, 0.499, 0.4999$ ; plane strain condition; loading: unit pressure at inner radius.

Table XVI. Normalized radial displacement at inner radius for a thick-walled cylinder (Figure 17).

Poisson's ratio $\mu$	Normalized radial displacement at inner radius				
	Q4	QUAD4 [3]	CPE4H [6]	CPE4I [6]	US-ATFQ4
0.49	0.845	0.846	0.994	0.986	<b>0.973</b>
0.499	0.359	0.359	0.994	0.986	<b>0.973</b>
0.4999	0.053	0.053	0.994	0.986	<b>0.973</b>

Data in bold are the results obtained by the models proposed in this paper.

It is well known that once some appropriate incompatible displacement modes (higher order displacements) are considered for a 4-node, 8-DOF plane membrane element, the element performance in nearly incompressible problems will be greatly improved, just like the results given in the Abaqus element CPE4I (Tables XV and XVI). It seems that the performance of the new unsymmetric element is strongly controlled by the second set of the assumed displacement fields, in which the pure bending (higher order displacements) modes in physical coordinates are introduced. Therefore, so long as the Poisson's ratio does not equal to 0.5, element US-ATFQ4 will also perform well in nearly incompressible problems. Furthermore, compared with elements formulated by isoparametric coordinates (such as CPE4I), element US-ATFQ4 is much more insensitive to mesh distortions. However, the theoretical and mathematical explanations still need further studies.

## 5. CONCLUDING REMARKS

In this paper, by combination of three advanced element techniques, including the unsymmetric element method, the QACM-II, and the analytical trial function method, a 4-node plane quadrilateral element US-ATFQ4 is successfully developed by a novel composite coordinate interpolation scheme. Numerical examples show that the new element is insensitive to various severe mesh distortions, free of the trapezoidal and the volumetric locking, and can satisfy both the classical first-order patch test and the second-order patch test for pure bending. Furthermore, because of usage of the QACM-II, the new element provides the invariance for the coordinate rotation. It seems that the present model completely breaks through the well-known contradiction defined by MacNeal's theorem [1, 2], that is, any 4-node, 8-DOF membrane element will either lock in in-plane bending or fail to pass a  $C_0$  patch test when the element's shape is an isosceles trapezoid. To date, it can hardly find any other similar 4-node, 8-DOF plane element, which can achieve all points described earlier.

Because the element stiffness matrix of the new element US-ATFQ4 is unsymmetric, the unsymmetric solvers, which may bring a few additional computation costs, are required. But this is not a serious issue in most of the problems in structural analyses [46–53]. Actually, in finite element analysis, strongly coupled problems and material nonlinearity may bring unsymmetry to the element matrices. So, the unsymmetric solvers have already been included in some finite element computer codes [68].

Cowan and Coombs [69] admitted the excellent performance of unsymmetric element (8-node plane element US-ATFQ8) with analytical trial functions in elasticity but claimed that it cannot be used in nonlinear problems. This conclusion may not be correct. Although the analytical trial functions come from the analytical solutions satisfying all governing equations for linear elasticity, but from the viewpoint of mathematics, they are only the combinations of physical coordinates with material constants. So long as an appropriate algorithm for updating coordinates and material constants is designed, such element should be able to extend to nonlinear applications. For example, by solving incremental form of the governing equations, the hybrid Trefftz finite element method, which is also based on the analytical solutions of elasticity, has already been successfully applied in various nonlinear problems [54, 70, 71].

Furthermore, how to extend this method to three-dimensional applications is another interesting and challenging topic. Although a three-dimensional hexahedral volume coordinate method (HVCN) corresponding to QACM-I has been proposed [72], it cannot be easily used because this HVCN contains six coordinate components. So, the most important thing is to establish a new HVCN (has only three coordinate components) corresponding to QACM-II and to find the basic analytical solutions in terms of the new HVCN.

In summary, there are still many challenging works that remain outstanding.

## APPENDIX A: THE DETAILED DERIVATION OF EQUATION (49)

For a plane finite element model, the virtual work principle [46] can be written as

$$\iint_{A^e} \delta \bar{\mathbf{e}}^T \hat{\boldsymbol{\sigma}}_t dA - \iint_{A^e} \delta \bar{\mathbf{u}}^T \mathbf{b}_t dA - \int_{\Gamma^e} \delta \bar{\mathbf{u}}^T \mathbf{T}_t ds - \delta \bar{\mathbf{u}}_c^T \mathbf{f}_c = 0, \quad (\text{A.1})$$

in which  $t$  is the thickness of the element;  $A^e$  is the element area;  $\Gamma^e$  is the element boundary;  $\hat{\sigma}$  is the real stress vector of the element;  $\mathbf{b}$ ,  $\mathbf{T}$ , and  $\mathbf{f}_c$  are the real body, the surface, and the concentrated forces of the element, respectively;  $\delta\bar{\mathbf{u}}_c$  is the vector of virtual displacements at the points of application of the concentrated forces;  $\delta\bar{\mathbf{u}}$  is the virtual displacement fields; and  $\delta\bar{\boldsymbol{\varepsilon}}$  is the corresponding virtual strain fields.

Two sets of the assumed displacement fields are considered.

The first set is the parametric displacement fields and given in Equation (29), and the corresponding strain fields are given in Equation (32). The assumed virtual displacements and strains will employ the same interpolation functions and can be written as

$$\delta\bar{\mathbf{u}} = \bar{\mathbf{N}}\delta\mathbf{q}^e, \quad (\text{A.2})$$

$$\delta\bar{\boldsymbol{\varepsilon}} = \bar{\mathbf{B}}\mathbf{q}^e, \quad (\text{A.3})$$

where  $\bar{\mathbf{N}}$  and  $\bar{\mathbf{B}}$  are given in Equations (30) and (33), respectively;  $\delta\mathbf{q}^e$  is the nodal virtual displacement vector. So, the virtual displacements are exactly compatible between two adjacent elements.

The second set of the assumed displacement and the corresponding strain fields are given in Equations (42) and (43), which can be rewritten as

$$\hat{\mathbf{u}} = \mathbf{P}\hat{\mathbf{d}}^{-1}\mathbf{q}^e, \quad (\text{A.4})$$

$$\hat{\boldsymbol{\varepsilon}} = \hat{\mathbf{B}}\mathbf{q}^e. \quad (\text{A.5})$$

Substitution of Equations (A.2), (A.3), and (A.5) into (A.1) yields

$$\begin{aligned} & \iint_{A^e} \delta\bar{\boldsymbol{\varepsilon}}^T \hat{\boldsymbol{\sigma}} t dA - \iint_{A^e} \delta\bar{\mathbf{u}}^T \mathbf{b} t dA - \int_{\Gamma^e} \delta\bar{\mathbf{u}}^T \mathbf{T} t ds - \delta\bar{\mathbf{u}}_c^T \mathbf{f}_c \\ &= \iint_{A^e} \delta\bar{\boldsymbol{\varepsilon}}^T \mathbf{D} \hat{\boldsymbol{\varepsilon}} t dA - \iint_{A^e} \delta\bar{\mathbf{u}}^T \mathbf{b} t dA - \int_{\Gamma^e} \bar{\mathbf{u}}^T \mathbf{T} t ds - \delta\bar{\mathbf{u}}_c^T \mathbf{f}_c \\ &= (\delta\mathbf{q}^e)^T \left( \iint_{A^e} \bar{\mathbf{B}}^T \mathbf{D} \hat{\mathbf{B}} \mathbf{q}^e t dA - \iint_{A^e} \bar{\mathbf{N}}^T \mathbf{b} t dA - \int_{\Gamma^e} \bar{\mathbf{N}}^T \mathbf{T} t ds - \bar{\mathbf{N}}_c^T \mathbf{f}_c \right), \\ &= (\delta\mathbf{q}^e)^T (\mathbf{K}^e \mathbf{q}^e - \mathbf{F}^e) \\ &= 0 \end{aligned} \quad (\text{A.6})$$

in which

$$\mathbf{K}^e = \iint_{A^e} \bar{\mathbf{B}}^T \mathbf{D} \hat{\mathbf{B}} t dA, \quad (\text{A.7})$$

$$\mathbf{F}^e = \iint_{A^e} \bar{\mathbf{N}}^T \mathbf{b} t dA + \int_{\Gamma^e} \bar{\mathbf{N}}^T \mathbf{T} t ds + \bar{\mathbf{N}}_c^T \mathbf{f}_c. \quad (\text{A.8})$$

Because of the arbitrariness of  $\delta\mathbf{q}^e$  in Equation (A.6), the following finite element equation can be obtained

$$\mathbf{K}^e \mathbf{q}^e - \mathbf{F}^e = \mathbf{0}, \quad (\text{A.9})$$

where  $\mathbf{F}^e$  is the nodal equivalent load vector of the element;  $\mathbf{K}^e$  is the element stiffness matrix of the unsymmetric element. Substitution of Equations (33) and (45) into (A.7) yields

$$\begin{aligned}\mathbf{K}^e &= \iint_{A^e} \bar{\mathbf{B}}^T \mathbf{D} \hat{\mathbf{B}} t dA = \int_{-1}^1 \int_{-1}^1 \frac{\bar{\mathbf{B}}^{*T}}{|\mathbf{J}|} \mathbf{D} \hat{\mathbf{B}} |\mathbf{J}| t d\xi d\eta \\ &= \int_{-1}^1 \int_{-1}^1 \bar{\mathbf{B}}^{*T} \mathbf{D} \hat{\mathbf{B}} t d\xi d\eta = \int_{-1}^1 \int_{-1}^1 \bar{\mathbf{B}}^{*T} \hat{\mathbf{S}} t d\xi d\eta \\ &= \int_{-1}^1 \int_{-1}^1 \bar{\mathbf{B}}^{*T} \hat{\mathbf{P}} \hat{\mathbf{d}}^{-1} t d\xi d\eta\end{aligned}\quad (\text{A.10})$$

Thus, Equation (49) is obtained.

#### ACKNOWLEDGEMENTS

The authors would like to acknowledge the financial supports of the National Natural Science Foundation of China (Project No. 11272181), the Specialized Research Fund for the Doctoral Program of Higher Education of China (Project No. 20120002110080), and Tsinghua University Initiative Scientific Research Program.

#### REFERENCES

1. MacNeal RH. A theorem regarding the locking of tapered four-noded membrane elements. *International Journal for Numerical Methods in Engineering* 1987; **24**(9):1793–1799.
2. MacNeal RH. On the limits of element perfectability. *International Journal for Numerical Methods in Engineering* 1992; **35**(8):1589–1601.
3. MacNeal RH, Harder RL. A proposed standard set of problems to test finite element accuracy. *Finite Elements in Analysis and Design* 1985; **1**(1):3–20.
4. Wilson EL, Taylor RL, Doherty WP, Ghabussi T. Incompatible displacement models. In *Numerical and Computer Methods in Structural Mechanics*, Fenven ST (ed.). Academic Press: New York, 1973; 43–57.
5. Taylor RL, Beresford PJ, Wilson EL. A non-conforming element for stress analysis. *International Journal for Numerical Methods in Engineering* 1976; **10**(6):1211–1219.
6. *Abaqus 6.9 HTML Documentation*. Dassault Systèmes Simulia Corp.: Providence, RI, USA, 2009.
7. Simo JC, Rifai MS. A class of mixed assumed strain methods and the method of incompatible modes. *International Journal for Numerical Methods in Engineering* 1990; **29**(8):1595–1638.
8. Pian THH, Sumihara K. Rational approach for assumed stress finite elements. *International Journal for Numerical Methods in Engineering* 1984; **20**(9):1685–1695.
9. Pian THH, Wu CC. *Hybrid and Incompatible Finite Element Methods*. Chapman & Hall/CRC: Boca Raton, 2006.
10. Wu CC, Huang MG, Pian THH. Consistency condition and convergence criteria of incompatible elements: general formulation of incompatible functions and its application. *Computers & Structures* 1987; **27**(5):639–644.
11. Yeo ST, Lee BC. New stress assumption for hybrid stress elements and refined four-node plane and eight-node brick elements. *International Journal for Numerical Methods in Engineering* 1997; **40**(16):2933–2952.
12. Sze KY. On immunizing five-beta hybrid stress element models from ‘trapezoidal locking’ in practical analyses. *International Journal for Numerical Methods in Engineering* 2000; **47**(4):907–920.
13. Cen S, Zhang T, Li CF, Fu XR, Long YQ. A hybrid-stress element based on Hamilton principle. *Acta Mechanica Sinica* 2010; **26**(4):625–634.
14. Long YQ, Cen S, Long ZF. *Advanced Finite Element Method in Structural Engineering*. Springer-Verlag GmbH: Berlin, Heidelberg; Tsinghua University Press: Beijing, 2009.
15. Chen WJ, Tang LM. Isoparametric quasi-conforming element. *Journal of Dalian University of Technology* 1981; **20**(1):63–74 (in Chinese).
16. Piltner R, Taylor L. A quadrilateral mixed finite element with two enhanced strain modes. *International Journal for Numerical Methods in Engineering* 1995; **38**(11):1783–1808.
17. Korelc J, Wriggers P. Improved enhanced strain four-node element with Taylor expansion of the shape functions. *International Journal for Numerical Methods in Engineering* 1997; **40**(3):407–421.
18. Lautersztajn SN, Samuelsson A. Further discussion on four-node isoparametric quadrilateral elements in plane bending. *International Journal for Numerical Methods in Engineering* 2000; **47**(1-3):129–140.
19. Piltner R, Taylor RL. A systematic constructions of B-bar functions for linear and nonlinear mixed-enhanced finite elements for plane elasticity problems. *International Journal for Numerical Methods in Engineering* 1999; **44**(5):615–639.
20. Rajendran S, Zhang BR. A “FE-meshfree” QUAD4 element based on partition of unity. *Computer Methods in Applied Mechanics and Engineering* 2007; **197**(1-4):128–147.

21. Xu JP, Rajendran S. A partition-of-unity based 'FE-Meshfree' QUAD4 element with radial-polynomial basis functions for static analyses. *Computer Methods in Applied Mechanics and Engineering* 2011; **200**(47-48): 3309–3323.
22. Lee NS, Bathe KJ. Effects of element distortion on the performance of isoparametric elements. *International Journal for Numerical Methods in Engineering* 1993; **36**(20):3553–3576.
23. Felippa CA. Supernatural QUAD4: a template formulation. *Computer Methods in Applied Mechanics and Engineering* 2006; **195**(41-43):5316–5342.
24. Fotiu PA. On shape sensitivity and patch test requirements of incompatible quadrilateral elements in physical coordinates. *Acta Mechanica* 2015; **226**(1):55–62.
25. Dasgupta G. Incompressible and locking free finite elements from Rayleigh mode vectors: quadratic polynomial displacement fields. *Acta Mechanica* 2012; **223**(8):1645–1656.
26. Dasgupta G. Locking free compressible quadrilateral finite elements: Poisson's ratio-dependent vector interpolants. *Acta Mechanica* 2014; **225**(1):309–330.
27. Long YQ, Li JX, Long ZF, Cen S. Area co-ordinates used in quadrilateral elements. *Communications in Numerical Methods in Engineering* 1999; **15**(8):533–545.
28. Long ZF, Li JX, Cen S, Long YQ. Some basic formulae for area co-ordinates used in quadrilateral elements. *Communications in Numerical Methods in Engineering* 1999; **15**(10):841–852.
29. Chen XM, Cen S, Fu XR, Long YQ. A new quadrilateral area coordinate method (QACM-II) for developing quadrilateral finite element models. *International Journal for Numerical Methods in Engineering* 2008; **73**(11): 1911–1941.
30. Long ZF, Cen S, Wang L, Fu XR, Long YQ. The third form of the quadrilateral area coordinate method (QACM-III): theory, application, and scheme of composite coordinate interpolation. *Finite Elements in Analysis and Design* 2010; **46**(10):805–818.
31. Chen XM, Cen S, Long YQ, Yao ZH. Membrane elements insensitive to distortion using the quadrilateral area coordinate method. *Computers & Structures* 2004; **82**(1):35–54.
32. Cen S, Chen XM, Fu XR. Quadrilateral membrane element family formulated by the quadrilateral area coordinate method. *Computer Methods in Applied Mechanics and Engineering* 2007; **196**(41-44):4337–4353.
33. Cen S, Du Y, Chen XM, Fu XR. The analytical element stiffness matrix of a recent 4-node membrane element formulated by the quadrilateral area coordinate method. *Communications in Numerical Methods in Engineering* 2007; **23**(10):1095–1110.
34. Du Y, Cen S. Geometrically nonlinear analysis with a 4-node membrane element formulated by the quadrilateral area coordinate method. *Finite Elements in Analysis and Design* 2008; **44**(8):427–438.
35. Cen S, Chen XM, Li CF, Fu XR. Quadrilateral membrane elements with analytical element stiffness matrices formulated by the new quadrilateral area coordinate method (QACM-II). *International Journal for Numerical Methods in Engineering* 2009; **77**(8):1172–1200.
36. Li G. A four-node plane parametric element based on quadrilateral area coordinate and its application to coupled solid-deformation/fluid-flow simulation for porous geomaterials. *International Journal for Numerical and Analytical Methods in Geomechanics* 2015; **39**(3):251–276.
37. Cardoso RPR, Yoon JW, Valente RAF. A new approach to reduce membrane and transverse shear locking for one-point quadrature shell elements: linear formulation. *International Journal for Numerical Methods in Engineering* 2006; **66**(2):1207–1223.
38. Cardoso RPR, Yoon JW, Valente RAF. Enhanced one-point quadrature shell element for nonlinear applications. *International Journal for Numerical Methods in Engineering* 2007; **69**(3):627–663.
39. Yoon JW, Cardoso RPR, Dick RE. Puncture fracture in an aluminum beverage can. *International Journal of Impact Engineering* 2010; **37**(2):150–160.
40. Wang Z, Sun Q. Corotational nonlinear analyses of laminated shell structures using a 4-node quadrilateral flat shell element with drilling stiffness. *Acta Mechanica Sinica* 2014; **30**(3):418–429.
41. Flajs R, Cen S, Saje M. On convergence of nonconforming convex quadrilateral finite elements AGQ6. *Computer Methods in Applied Mechanics and Engineering* 2010; **199**(25-28):1816–1827.
42. Cardoso RPR, Yoon JW. One point quadrature shell elements: a study on convergence and patch tests. *Computational Mechanics* 2007; **40**(5):871–883.
43. Prathap G, Senthilkumar V. Making sense of the quadrilateral area coordinate membrane elements. *Computer Methods in Applied Mechanics and Engineering* 2008; **197**(49-50):4379–4382.
44. Chen XM, Cen S, Li YG, Sun JY. Several treatments on non-conforming element failed in the strict patch test. *Mathematical Problems in Engineering* 2013; **2013**(90):1495.
45. Prathap G. Stay Cartesian, or go natural? A comment on the article "Supernatural QUAD4: a template formulation" by C. A. Felippa [Comput. Methods Appl. Mech. Engrg., 195 (2006) 5316–5342]. *Computer Methods in Applied Mechanics and Engineering* 2007; **196**(9-12):1847–1848.
46. Rajendran S, Liew KM. A novel unsymmetric 8-node plane element immune to mesh distortion under a quadratic displacement field. *International Journal for Numerical Methods in Engineering* 2003; **58**(11):1713–1748.
47. Rajendran S. A technique to develop mesh-distortion immune finite elements. *Computer Methods in Applied Mechanics and Engineering* 2010; **199**(17-20):1044–1063.
48. Liew KM, Rajendran S, Wang J. A quadratic plane triangular element immune to quadratic mesh distortions under quadratic displacement fields. *Computer Methods in Applied Mechanics and Engineering* 2006; **195**(9-12): 1207–1223.

49. Ooi ET, Rajendran S, Yeo JH. A 20-node hexahedral element with enhanced distortion tolerance. *International Journal for Numerical Methods in Engineering* 2004; **60**(14):2501–2530.
50. Ooi ET, Rajendran S, Yeo JH. Extension of unsymmetric finite elements US-QUAD8 and US-HEXA20 for geometric nonlinear analyses. *Engineering Computations* 2007; **24**(4):407–431.
51. Rajendran S, Ooi ET, Yeo JH. Mesh-distortion immunity assessment of QUAD8 elements by strong-form patch tests. *Communications in Numerical Methods in Engineering* 2007; **23**(2):157–168.
52. Ooi ET, Rajendran S, Yeo JH. Remedies to rotational frame dependence and interpolation failure of US-QUAD8 element. *Communications in Numerical Methods in Engineering* 2008; **24**(11):1203–1217.
53. Cen S, Zhou GH, Fu XR. A shape-free 8-node plane element unsymmetric analytical trial function method. *International Journal for Numerical Methods in Engineering* 2012; **91**(2):158–185.
54. Qin QH. Trefftz finite element method and its applications. *Applied Mechanics Reviews* 2005; **58**(5):316–337.
55. Cen S, Fu XR, Zhou MJ. 8- and 12-node plane hybrid stress-function elements immune to severely distorted mesh containing elements with concave shapes. *Computer Methods in Applied Mechanics and Engineering* 2011; **200**(29-32):2321–2336.
56. Cen S, Fu XR, Zhou GH, Zhou MJ, Li CF. Shape-free finite element method: the plane hybrid stress-function (HS-F) element method for anisotropic materials. *Science China Physics, Mechanics & Astronomy* 2011; **54**(4):653–665.
57. Cen S, Zhou MJ, Fu XR. A 4-node hybrid stress-function (HS-F) plane element with drilling degrees of freedom less sensitive to severe mesh distortions. *Computers & Structures* 2011; **89**(5-6):517–528.
58. Cen S, Zhou MJ, Shang Y. Shape-free finite element method: another way between mesh and mesh-free methods. *Mathematical Problems in Engineering* 2013; **2013**(49):1626.
59. Zhou MJ, Cen S, Bao Y, Li CF. A quasi-static crack propagation simulation based on shape-free hybrid stress-function finite elements with simple remeshing. *Computer Methods in Applied Mechanics and Engineering* 2014; **275**:159–188.
60. Zhou PL, Cen S. A novel shape-free plane quadratic polygonal hybrid stress-function element. *Mathematical Problems in Engineering* 2015; **2015**(49):1325.
61. Cook RD. Improved two-dimension finite element. *Journal of the Structural Division (ASCE)* 1974; **100ST9**:1851–1863.
62. Andelfinger U, Ramm E. EAS-elements for two-dimensional, three-dimensional, plate and shell structures and their equivalence to HR-elements. *International Journal for Numerical Methods in Engineering* 1993; **36**(8):1311–1337.
63. MacNeal RH, Harder RL. A refined four-noded membrane element with rotation degrees of freedom. *Computers & Structures* 1988; **28**(1):75–84.
64. Ibrahimovic A, Taylor RL, Wilson EL. A robust quadrilateral membrane element with rotational degrees of freedom. *International Journal for Numerical Methods in Engineering* 1990; **30**(3):445–457.
65. Timoshenko SP, Goodier JN. *Theory of Elasticity* (3rd edn). McGraw-Hill: New York, 1934.
66. Spilker RL, Maskeri SM, Kania E. Plane isoparametric hybrid-stress elements: invariance and optimal sampling. *International Journal for Numerical Methods in Engineering* 1981; **17**(10):1469–1496.
67. Cook RD, Malkus DS, Plesha ME. *Concepts and Applications of Finite Element Analysis* (3rd edn). John Wiley & Sons, Inc.: New York, 1989.
68. *INTESIM 2014 Theory Manual*. Intesim Group: Venetia, PA, USA, 2014.
69. Cowan T, Coombs WM. Rotationally invariant distortion resistant finite-elements. *Computer Methods in Applied Mechanics and Engineering* 2014; **275**:189–203.
70. Qin QH. Nonlinear analysis of thick plates by HT FE approach. *Computers & Structures* 1996; **61**(2):271–281.
71. Qin QH. Formulation of hybrid Trefftz finite element method for elastoplasticity. *Applied Mathematical Modelling* 2005; **29**(3):235–252.
72. Li HG, Cen S, Cen ZZ. Hexahedral volume coordinate method (HVCM) and improvements on 3D Wilson hexahedral element. *Computer Methods in Applied Mechanics and Engineering* 2008; **197**(51-52):4531–4548.